NUMERICAL INVESTIGATION OF EFFECTS OF PRESSURE AND CHEMISTRY ON CHARACTERISTICS OF TURBULENT PREMIXED FLAMES

By

Jamie L. Bowers

Reetesh Ranjan
Assistant Professor
(Advisor)

Kidambi Sreenivas
Professor
(Committee Member)

Charles Margraves
UC Foundation Associate Professor
(Committee Member)

NUMERICAL INVESTIGATION OF EFFECTS OF PRESSURE AND CHEMISTRY ON CHARACTERISTICS OF TURBULENT PREMIXED FLAMES

By

Jamie L. Bowers

A Thesis Submitted to the Faculty of the University of
Tennessee at Chattanooga in Partial
Fulfillment of the Requirements of the Degree
of Master of Engineering

The University of Tennessee at Chattanooga
Chattanooga, Tennessee

August 2021

ABSTRACT

Turbulent premixed flames are used in many energy conversion and propulsion devices. The efficiency and performance of these devices are affected by operating conditions, which also affect the highly nonlinear turbulence-chemistry interactions (TCIs). Previous fundamental studies characterize TCIs at atmospheric pressure, but relevant devices usually operate at higher pressures. This study investigates the effects of elevated pressure and finite-rate chemistry on methane/air turbulent premixed flames using direct numerical simulations performed at pressures of 1 atm and 10 atm and utilize an 8-species and 4-steps mechanism and a 13-species and 73-steps mechanism. The effects of pressure and chemistry on TCIs are examined in terms of the statistical and spectral features. At elevated pressure, there is more flame-front wrinkling, affecting flame curvature and heat release rate. The smaller length scales of turbulence become more energetic, and TCIs are more sensitive to finite-rate chemistry, indicating that complex chemical models may be more appropriate.

ACKNOWLEDGEMENTS

I want to offer my overwhelming gratitude to my research supervisor and thesis advisor, Dr. Reetesh Ranjan, for his invaluable professional and academic guidance. It has been a privilege to work under his supervision, and completing my thesis would not have been possible without his support. I'd also like to extend my sincere thanks to my committee members, Dr. Kidambi Sreenivas and Dr. Charles Margraves, for their continued support throughout my time at UTC. I am deeply grateful to Dr. Prakash Dhamshala, whose encouragement played an essential role in my decision to pursue graduate studies.

I want to thank the Fluids and Combustion Modeling group members, specifically Eli Durant and Jash Doshi, for their unwavering help during the writing of this thesis. A special thanks to the UTC College of Engineering and Computer Science's technical and administrative staff, particularly Ms. Andrea James, whose help cannot be overestimated. I gratefully acknowledge the support of the SimCenter: Center of Excellence in Applied Computational Science and Engineering (CEACSE) grant from the University of Tennessee at Chattanooga for funding this research and providing the computational resources and technical support.

TABLE OF CONTENTS

LIST OF FIGURES

LIST OF TABLES

LIST OF ABBREVIATIONS

DNS, Direct numerical simulation

LES, Large-eddy simulation

FVM, Finite volume method

MPI, Message passing interface

WF, Wrinkled flamelet regime

CF, Corrugated flamelet regime

TRZ, Thin reaction zone regime

B/DRZ,Broken/distributed reaction zone regime

BP-TR, Broadened preheat-thin reaction layer regime

SGS, Subgrid-scale

HRR, Heat release rate

PDF, Probability density function

HPC, High-performance computing

RAM, Random-access memory

SKE, Spectral kinetic energy

TCIs, Turbulence-chemistry interactions

LIST OF SYMBOLS

l_t, integral length scale

η, Kolmogorov length scale

i, Cartesian coordinate directions

x_i, position

u_i, velocity

ρ, density

p, pressure

T, temperature

τ_{ij}, viscous stress tensor

N_s, total number of species

Y_k, mass fraction of the k^{th} species

$V_{k,i}$, diffusion velocity of the k^{th} species

$\dot{\omega}_k$, reaction rate of the k^{th} species

W_k, molecular weight of the k^{th} species

R, mixture gas constant

R_u, universal gas constant

e, specific internal energy

h, specific enthalpy

$\Delta h^{\circ}_{f,k}$, enthalpy of formation

$c_{p,k}$, specific heat at constant pressure for the k^{th} species

$c_{v,k}$, specific heat at constant volume for the k^{th} species

R_k, gas constant for the k^{th} species

τ_{ij}, viscous stress tensor

q_i, heat-flux vector

S_{ij}, strain-rate tensor

δ_{ij}, Kronecker delta

W, mixture molecular weight

D_k, diffusion coefficient of the k^{th} species

X_k, mole fraction of the k^{th} species

L, length of the domain

p_{ref}, reference pressure

T_{ref}, reference temperature

ϕ, equivalence ratio

u', turbulence intensity

S_{L}, laminar flame speed

δ_{L}, laminar thermal flame thickness

u'/S_{L}, characteristic velocity scale ratio

l_t/δ_{L}, characteristic length scale ratio

Re, integral Reynolds number

Ka, Karlovitz number

Da, Damköhler number

T_{b}, temperature in the burnt regions

T_{u}, temperature in the unburnt regions

T_{ad}, adiabatic flame temperature

N_i, spatial grid resolution

k_{max}, largest wave number

$t_0 = l_t/u'$, initial eddy turnover time

c, progress variable

$||\boldsymbol{\omega}||$, vorticity magnitude

x_0, mean global flame position

Ω, computational domain

κ, flame curvature

$\mathbf{n}$, unit normal vector of the flame front

μ, mean

σ , standard deviation

γ, skewness

$\mathcal{T}_i$, nonlinear advection term

$\mathcal{P}_i$, pressure gradient effects term

$\mathcal{V}_i$, shear viscous diffusion term

$\mathcal{D}_i$, dilatational viscous effects term

k_p, two-dimensional wave vector

$\widehat{E}$, spectral kinetic energy

λ, thermal conductivity

CHAPTER 1

INTRODUCTION

Turbulent premixed combustion is observed in several engineering devices such as internal combustion engines, gas turbines, and swirl combustors. Such systems are typically operated under high pressure, lean conditions, and intense turbulent environments [12, 44] to have higher efficiency, compact design, and better emissions characteristics. The highly nonlinear turbulence-chemistry interactions prevalent in such devices are a multi-scale phenomenon [16, 30, 32]. The interplay of various processes such as reaction, molecular mixing, convective processes, and thermal expansion occurs within the flame. Many of these processes are still unsolved fundamental problems in combustion research.

There are different types of fluid flows, but the most common types encountered are the laminar and turbulent flow regimes. Turbulent flow is fluid motion characterized by chaotic changes in pressure and flow velocity. Turbulent flows are found in nature, such as rivers, natural convection, and even blood flow in arteries. However, turbulent flows also occur in many applications, such as in the study of aerodynamics, and it is used to increase heat transfer in pipes, ducts, and heat exchangers.

All types of flows can be classified as reactive or non-reactive flows. Reactive flows are flows with chemical reactions taking place. Such flows are used in many applications such as detonations, propulsion devices, combustion, and even astrophysics. These flows

are governed by the conservation of mass, momentum, and energy and the conservation of species mass. Before reaching chemical equilibrium, chemical reactions often undergo many elementary reactions generating intermediate species (radicals). There can be hundreds of elementary reactions and intermediate species in combustion reactions, making modeling difficult, especially in turbulent combustion. This difficulty is due to highly nonlinear interactions between turbulence and chemistry, known as turbulence-chemistry interactions (TCIs).

Combustion can be classified into three modes: premixed, non-premixed, and partially premixed. Premixed combustion occurs when fuel and oxidizer are mixed before any reaction takes place. In non-premixed combustion, the fuel and oxidizer are not mixed before reaction, and in partially-premixed combustion, the fuel and oxidizer are incompletely mixed before reaction. The focus of the present study is premixed combustion occurring within a turbulent environment.

Turbulent premixed flames have been extensively investigated in the past through experimental, theoretical, and computational approaches to characterize their temporal, spatial, topological, statistical, and spectral characteristics. In such flames, the interaction between turbulence and chemistry is interdependent. For example, the presence of flame and the associated heat release and thermal expansion affects the characteristics of turbulence by modifying the length scales of the eddies, and on the other hand, the energetic turbulent eddies lead to stretching and wrinkling of the flame surface.

The multi-scale nature of the TCIs makes it extremely challenging to predict their characteristics in practically relevant scenarios, thus necessitating further fundamental studies to characterize their behavior under practically relevant operating conditions. The present study focuses on examining the effects of pressure and finite-rate chemistry on the features of turbulent premixed flames by performing high-fidelity simulations of a canonical turbulent premixed flame configuration.

Premixed flames are topologically characterized into distinct zones. The first zone is the unburned zone containing the unburnt reactant mixture, and the last zone is the burned gas zone, or post-flame zone, characterized by high temperatures and chemical equilibrium. The transition between the unburnt and burnt states occurs within the flame brush, which comprises of the preheat and reaction zones. The preheat zone begins when the temperature starts to rise and ends at the ignition temperature. The end of the preheat zone indicates the beginning of the reaction zone, where fuel and oxidizer are converted to products.

Due to the presence of multiple spatial and temporal scales, turbulent premixed flames are classified into different regimes, namely, wrinkled flamelets (WF), corrugated flamelets (CF), thin reaction zone (TRZ) and broken/distributed reaction zone (B/DRZ) [30, 32]. Recent experimental studies have also characterized the existence of another regime, referred to as the broadened preheat-thin reaction (BP-TR) layer for flames under extreme turbulence [48]. The key parameters for classification of regimes are: turbulence intensity (u'), laminar flame speed (S_{L}), integral length scale (l_t), and the flame thickness (δ_{L}). A detailed description of the regime diagram for premixed flames and its different variations are presented

elsewhere [30, 32]. These regimes can also be characterized in terms of non-dimensional numbers, such as Karlovitz number (Ka), Reynolds number (Re), and Damköhler number (Da). The turbulent premixed flames considered in this study correspond to the TRZ and B/DRZ regimes, therefore the key features of these regimes are summarized below.

The TRZ regime is characterized by $1 < Ka < Ka_c$, where $Ka_c \approx 100$. In this regime, the preheat zone gets thickened by the eddies, but the reaction zone remains unaffected as the small-size eddies get dissipated before they can disrupt the reaction zone [46]. Some other features of this regime include increased wrinkling of the flame surface, enhanced heat and mass transport, and an increase in fuel consumption compared to the unstretched laminar flame. In the B/DRZ regime ($Ka > Ka_c$), the transport by energetic turbulent eddies dominates differential diffusion, and therefore, can potentially lead to local/global extinction [30]. Some of the experimental and numerical studies of such flames have shown that local extinction can occur for $Ka \gg Ka_c$ due to gas expansion across the flame region [2, 12, 24, 27, 39]. Flames in this regime also exhibit a diffused interface between fuel and products with the flame structure resembling a turbulent mixing zone. Experimental studies of methane/air flames in TRZ and B/DRZ regimes have shown that an increase in the turbulence intensity manifests as a progressive broadening of the flame brush [7, 11, 12, 27, 47, 60]. However, recent investigations of the flame structure under intense turbulence [40, 47, 48] have shown the presence of a continuous and constant fuel-consumption layer, thus precluding the presence of local/global extinction.

As stated before, turbulence-chemistry interactions are highly nonlinear, and as a result, the role of finite-rate chemistry becomes important. It has been suggested that many turbulent flame characteristics are insensitive to the complexity of the chemical mechanism employed in computational studies [23]. Still, other studies have shown the effects of chemical models on turbulence-chemistry interactions [29]. Nevertheless, many previous computational studies employed reduced chemical models to offset computational costs related to the use of complex chemical models while employing the finite-rate chemistry approach.

Although the behavior of turbulent premixed flames has been well characterized, many of these past studies are performed usually at atmospheric pressure, whereas the practically relevant combustion devices operate at higher pressure. Recent computational and experimental studies have shown that a variation in pressure directly affects the flame characteristics [1, 8, 15, 19, 20, 22, 25, 50–54, 58], and more complex chemical mechanisms may be needed to capture these effects effectively [53, 58]. Therefore, further studies are required to contribute to the understanding and characterization of the effects of pressure and finite-rate chemistry at elevated pressure, a vital step in developing predictive models.

The present study focuses on the computational investigation of turbulent premixed flames under high-pressure conditions through high-fidelity simulations. Direct numerical simulation (DNS) of turbulent premixed flames [2, 29, 33–35, 46, 49] is typically used to examine fundamental features of such flames, and therefore is considered in this study. Note that DNS is typically limited to canonical configurations due to its prohibitive computational cost for practical applications operating at high Re. For practical configurations, large eddy

simulation (LES) tends to be a viable alternative, where the large-scales are resolved, and the effects of the subgrid-scale (SGS) turbulence-chemistry interaction are modeled [31]. In terms of the chemistry modeling, the cost associated with compressible finite-rate chemistry using detailed kinetics still tends to be huge when it comes to simulation of practical combustion devices due to a large number of transport equations and tedious calculations associated with the evaluation of transport and thermodynamic properties. Therefore, we consider the use of moderately complex and skeletal chemical kinetics to demonstrate the effects of the employed chemical models on the characteristics of flames considered in this study.

The cases in this study are simulated at pressures of 1 atm and 10 atm and correspond to the TRZ and B/DRZ regimes. In total, four cases are simulated using two different chemical mechanisms to examine the effects of the complexity of chemical models while employing a finite-rate chemistry approach. Specifically, we employ a moderately complex 8-species and 4-step mechanism and a skeletal 13-species and 73-step mechanism. The results from the DNS of the cases are used to examine the flame-turbulence interactions comprehensively in terms of the effects of pressure and chemistry on the spatial, statistical, and spectral features.

1.1 Key Technical Objectives

This thesis aims to contribute to the fundamental understanding of the effects of pressure and chemistry on the features of turbulent premixed flames by meeting the following key objectives:

- **Characterize the effects of pressure on structural, statistical, and spectral features:** Most past studies have focused on characterizing turbulence-flame interactions at atmospheric pressure, but practically relevant engineering devices usually operate at high pressures. Therefore, a fundamental understanding of how pressure affects the behavior of turbulent premixed flame is an essential step in developing predictive turbulent combustion models to study practical devices. In particular, the effects of variation in pressure are examined in terms of the flame topology, spatial, single point, and conditional statistics, and through two-dimensional spectral analysis. A key focus is to characterize the behavior of the flame curvature, heat release rate (HRR), and their correlation as the pressure is varied. Furthermore, at elevated pressure, the effects of variation in the velocity and the length scale ratios are considered.

- **Characterize the effects of finite-rate chemistry on structural, statistical, and spectral features:** Intermediate species in a numerical system can increase computational cost due to an increased number of species transport equations and the associated stiffness of the governing equations. As a result, most previous computational studies employed simpler chemical models to reduce computational costs. However, it has recently been hypothesized that local chemical pathways may also be sensitive to the effects of pressure [53] and fast chemistry assumptions may not be valid for high operating pressures [58]. Therefore, we employ a moderately complex 8-species and 4-step mechanism [41], and skeletal 13-species and 73-step mechanism [36] to investigate how the complexity of the chemical mechanism affects the characteristic features

of turbulence-chemistry interactions. Furthermore, both mechanisms are employed at pressures of 1 atm and 10 atm to identify how these effects vary at elevated pressure. In particular, the effects of finite-rate chemistry are discussed in terms of the flame topology, spatial, single point, and conditional statistics, and through two-dimensional spectral analysis.

1.2 Thesis Layout

This thesis is divided into seven chapters including this introductory chapter. First, the current state-of-the-art for research on turbulent premixed flames under intense turbulence conditions and at elevated pressure is reviewed in Chapter 2. Next, the governing equations and numerical methodology are described in Chapter 3. Afterward, the details of the computational setup and a description of the cases considered in this study are presented in Chapter 4. A comprehensive analysis of the effects of pressure and chemical models while employing the finite-rate chemistry strategy are discussed in Chapter 5 and Chapter 6, respectively. Finally, the key findings and future directions are summarized in Chapter 7.

CHAPTER 2

TURBULENT PREMIXED FLAMES AT ELEVATED PRESSURE

Turbulent premixed flames are used in many energy conversion and propulsion devices such as gas turbines, internal combustion engines, and swirl combustors. The efficiency and performance of these kinds of devices are significantly affected by the operating conditions, which in turn affect the highly nonlinear turbulence-chemistry interactions. Past fundamental studies have focused on characterizing the behavior of such interactions under a wide range of operating conditions. However, most of these studies are performed at atmospheric pressure, whereas the practically relevant combustion devices usually operate at much higher pressures. Therefore, a fundamental understanding of how pressure affects the behavior of turbulent premixed flames is an important step in developing predictive turbulent combustion models to study practical devices.

In this chapter, the key features of turbulent premixed flames established in past studies are briefly summarized. A detailed survey of characteristics of such flames is presented in the review articles [5, 9, 10, 43]. Here, we focus on turbulent premixed flames under intense turbulence conditions and summarize the behavior of such flames at atmospheric and elevated pressure conditions.

2.1 Features of Flames at Atmospheric Pressure

In recent years, DNS has been extensively used to investigate the fundamental features of turbulent premixed flames. In particular, the structural and statistical characteristics of turbulent premixed flames have been widely investigated over the past few decades and continues to be a growing area of research [5, 10, 43]. Recent studies using DNS have focused on the study of turbulent premixed flames under lean conditions and intense turbulent environments [2, 12, 39, 44] as such conditions are known to yield stable combustion and better emissions characteristics.

A key feature of such flames is the modification of the flame structure by the turbulent eddies, particularly a progressive broadening of the preheat zone. It is also hypothesized that at extreme levels of turbulence, the reaction zone may also get disrupted leading to local/global extinction [2, 11, 12, 24, 27, 30, 39]. For example, Aspden et al. [2] conducted DNS to investigate the effects of turbulence on premixed flames and characterized the B/DRZ regime. The study concluded that increasing turbulence intensity leads to a more disturbed flame structure and increased peak local burning rate and turbulent flame speeds. Furthermore, the study found that flames in the B/DRZ regime have a less sharp interface between fuel and products. Savre et al. [39] used two-dimensional DNS of methane/air turbulent premixed flames to examine the effects of turbulence on the inner flame structure. The study showed that an increase in the turbulence intensity leads to large, protruding structures and a broader heat release layer. In addition to this, the study reported that flames in the B/DRZ regime are broader, have temperatures that change linearly with the progress variable, and

the peak mass fractions of minor species are less than predicted by laminar flames. Flames under high level of background turbulence also exhibit a diffused interface between fuel and products with the flame structure resembling a turbulent mixing zone [7, 11, 12, 27, 47, 60]. Recent investigations of such flames [40, 47, 48] have shown the presence of a continuous and constant fuel-consumption layer, thus precluding the presence of local/global extinction.

Turbulence-chemistry interactions are highly nonlinear, and therefore, the role of finite-rate chemistry is key to such interactions, which has also been investigated in past studies. Carlsson et al. [3, 4] conducted DNS of premixed methane and hydrogen flames to investigate the effects of turbulence on the flame structures. Their results showed that differential diffusion has a significant impact on the flame structure at high turbulence levels, and single-step chemistry does not capture the role of differential diffusion. Lapointe and Blanquart [23] used direct numerical simulations to investigate the effects of chemistry further. They compared a wide range of fuel types, chemical mechanisms, and equivalence ratios. They found that the turbulent flame speed and fuel consumption rates are relatively insensitive to the chemical model. Furthermore, they suggest that regardless of the chemical model used, turbulent flame behavior can be accurately predicted by knowing only a few laminar flame properties, such as laminar flame speed, laminar flame thickness, reaction zone thickness, and the fuel Lewis number to model differential diffusion.

These contributions have provided the foundations for current research but are limited because only turbulent premixed flames at atmospheric pressure were studied. Practical combustion devices operate at much higher pressures, and therefore further studies are needed

to characterize the behavior of turbulence-chemistry interactions at elevated pressure and intense turbulence conditions. The expensive and risky nature of experimental research for premixed combustion makes DNS a better alternative to carrying out fundamental studies.

2.2 Features of Flames at Elevated Pressure

Turbulent premixed flames at elevated pressure have gained significant interest recently, and progress has been made to describe the effects of pressure on various characteristics of turbulent premixed flames. This section summarizes the key observations from experimental and computational studies of turbulent premixed flames at elevated pressure.

2.2.1 Experimental Observations

Lachaux et al. [22] investigated the flame front of methane/air turbulent premixed flames using an experimental Bunsen flame setup at pressures of up to about 9 atm. Their results show that laminar flame speed (S_{L}) decreases with increasing pressures, leading to an increase in the characteristic velocity scale ratio (u'/S_{L}). They also reported increased flame surface density and burning rates with higher pressures and observed more small-scale flame structures at elevated pressures. Kobayashi et al. [20] examined the effects of increasing pressure and temperature on turbulent burning velocities by using a Bunsen-type flame setup and testing pressures up to around 10 atm. Their results showed that the ratio of turbulent and laminar burning velocities is significantly affected by pressure.

The structural features of flames at high pressures have also been experimentally investigated. Wang et al. [51] investigated the effects of fuel dilution at high temperatures

and pressures. Their experiment revealed a more general conclusion that turbulent premixed flame fronts are significantly more wrinkled at high temperatures and high pressures. Wang et al. [52] used a nozzle-type Bunsen burner to experimentally analyze the effects of elevated pressure on turbulent premixed flames at pressures up to about 10 atm. They reported that at elevated pressure the flame front has many small-scale cusps superimposed with large-scale flame branches, and their results also show that the burning velocity ratio and characteristic velocity scale ratio increase with pressure. Fragner et al. [15] investigated the effects of pressure even further in Bunsen flames. Their experimental setup tested the Bunsen flames with pressures up to 5 atm. They determined that increasing pressure causes the energy spectrum to stretch further in the direction of small scales and high wavenumbers. They also reported that the curvature distribution broadens if the laminar flame thickness (δ_{L}) is constant during pressure increases. Recently, Wang et al. [50] came to the same conclusion about curvature experimentally. Their study showed that the increase in pressure leads to a more flat and broad probability density function of curvature.

2.2.2 Computational Observations

In addition to experimental studies, there has been a growing body of DNS studies that analyze the effect of elevated pressure on turbulent premixed flames. Yilmaz and Gokalp [58] used DNS and experiments to investigate the effects of high pressures on the turbulent premixed flame structure. They used pressures of up to about 9 atm and determined that flame speed decreases with increasing pressure, whereas thicker flame brushes were observed at high pressures, and there is a downstream shift of the flame front location. They also

concluded that a fast chemistry assumption might not be valid at high pressures. Dinesh et al. [8] used three-dimensional DNS to examine the effects of pressures up to around 4 atm. Their results showed that as pressure is increased, the reaction zone becomes thin and more wrinkled. This leads to higher negative and positive curvature zones, and the effects caused by elevated pressure on heat release rate (HRR) are more significant than the effects caused by variations in the turbulence intensities.

Wang et al. [53, 54] used three-dimensional DNS to investigate the effects of pressure on flame structures and chemical pathways for turbulent premixed hydrogen flames. They reported that under quasi-constant turbulence intensity conditions, the flame fronts at elevated pressures have sharper structures, and heat release is enhanced in the concave areas. Additionally, they reported an increase in the probability of high curvature and a reduction in the decorrelation of HRR and fuel consumption rate at elevated pressures. Klein et al. [19] used DNS to analyze the flame curvature statistics of turbulent premixed Bunsen flames at pressures up to about 10 atm. Their results showed that increasing pressure while maintaining a constant velocity scale ratio causes cusp formation and increases skewness of the flame curvature PDF. They also reported that increasing pressure leads to a broader PDF of flame curvature, which indicated an increase in small-scale flame front wrinkling.

Alqallaf et al. [1] used three-dimensional DNS to investigate flame curvature in turbulent premixed Bunsen flames at elevated pressures. Their results show that at elevated pressures, there is a higher probability of developing large negative curvature. Finally, Lu and Yang [25] proposed a predictive model for the turbulent burning velocity over a range

of pressures and turbulence intensities. They cited the increase in the ratio of turbulent and laminar burning velocities as the motivation for developing the model.

2.3 Summary

High-pressure conditions affect several characteristics of both laminar and turbulent premixed flames. At elevated pressures, the laminar flame speed and flame thickness decrease, the reaction zone is thinner, and the flame front location shifts further downstream, leading to thicker flame brushes. Elevated pressures produce more wrinkled flame fronts with sharper structures under turbulent conditions. Increasing pressure also affects the characteristics of maximum HRR and flame curvature. In particular, high pressure leads to higher maximum heat release rates, and the maximum HRR values move from lower temperatures to higher temperatures. In addition to this, the decorrelation of heat release and fuel consumption is reduced at high pressures. As pressure increases, the probability density function (PDF) distribution of flame curvature broadens and becomes flatter. The broadening of the PDF indicates a higher probability for large magnitude curvature and enhancement of small-scale flame front wrinkling.

CHAPTER 3

MATHEMATICAL FORMULATION AND NUMERICAL METHODOLOGY

In this chapter, the governing equations and the numerical approach employed to solve the equations are described.

3.1 Governing Equations

We consider a fully compressible formulation with finite-rate chemistry to describe the turbulent premixed flames considered in this study. The governing equations comprise the compressible multi-species reacting Navier-Stokes equations, which correspond to the conservation of mass, momentum, energy, and species mass. These equations are given by

$$\frac{\partial \rho}{\partial t} + \frac{\partial \rho u_i}{\partial x_i} = 0, \tag{3.1.1a}$$

$$\frac{\partial \rho u_i}{\partial t} + \frac{\partial}{\partial x_j}\left[\rho u_i u_j + p\delta_{ij} - \tau_{ij}\right] = 0, \tag{3.1.1b}$$

$$\frac{\partial \rho E}{\partial t} + \frac{\partial}{\partial x_i}\left[(\rho E + p)u_i + q_i - u_j\tau_{ij}\right] = 0, \tag{3.1.1c}$$

$$\frac{\partial \rho Y_k}{\partial t} + \frac{\partial}{\partial x_i}\left[\rho Y_k\left(u_i + V_{k,i}\right)\right] = \dot{\omega}_k, \qquad k = 1, ..., N_s. \tag{3.1.1d}$$

Here, ρ is the density, $(u_i)_{i=1,2,3}$ is the velocity component in the Cartesian coordinates, p is the pressure, τ_{ij} is the the viscous stress tensor, and Y_k, $V_{k,i}$, and $\dot{\omega}_k$ are the mass fraction, diffusion velocity component, and reaction rate of the k^{th} species, respectively.

Also, N_s is the total number of species in the flow. The above governing equations (3.1.1) are closed by the thermally perfect gas equation of state

$$p = \rho R T, \tag{3.1.2}$$

where, R is the mixture gas constant, which is given by

$$R = \sum_{k=1}^{N_s} Y_k \frac{R_u}{W_k}, \tag{3.1.3}$$

where, R_u is the universal gas constant and W_k is molecular weight of the k^{th} species. Using the thermally perfect gas equation of state, the specific internal energy e is given by

$$e = \sum_{k=1}^{N_s} Y_k e_k = \sum_{k=1}^{N_s} Y_k \int_{T_0}^{T} c_{v,k}(T) dT, \tag{3.1.4}$$

and the specific enthalpy h is given by

$$h = \sum_{k=1}^{N_s} Y_k h_k = \sum_{k=1}^{N_s} Y_k \left(\int_{T_0}^{T} c_{p,k}(T) dT + \Delta h^{\circ}_{f,k} \right). \tag{3.1.5}$$

Here, $c_{p,k}$, $c_{v,k}$, R_k, and $\Delta h^{\circ}_{f,k}$ are the specific heat at constant pressure, constant volume, gas constant, and the enthalpy of formation, respectively, for the k^{th} species. The temperature dependent $c_{p,k}$ is obtained from classical temperature curve-fits and $c_{p,k} = c_{v,k} + R_k$.

The viscous stress tensor, τ_{ij}, and the heat-flux vector, q_i are given by

$$\tau_{ij} = 2\mu(T)\left(S_{ij} - \frac{1}{3}S_{kk}\delta_{ij}\right), \tag{3.1.6}$$

$$q_i = -\lambda(T)\frac{\partial T}{\partial x_i} + \rho\sum_{k=1}^{N_s} h_k Y_k V_{i,k}, \tag{3.1.7}$$

where, $S_{ij} = \frac{1}{2}\left(\frac{\partial u_i}{\partial x_j} + \frac{\partial u_j}{\partial x_i}\right)$ is the strain-rate tensor, λ is the thermal conductivity, and μ is the dynamic viscosity. The diffusion velocity $V_{k,i}$ for the k^{th} species is given by

$$V_{k,i} = -D_k\frac{1}{X_k}\frac{\partial X_k}{\partial x_i} + \frac{1}{W}\sum_{k=1}^{N_s} D_k W_k\frac{\partial X_k}{\partial x_i}, \tag{3.1.8}$$

where, W is the mixture molecular weight, and D_k and X_k are diffusion coefficient and mole fraction of the k^{th} species, respectively. The diffusion coefficient for a species is obtained through the well-known mixture-averaged formulation [32]. The above system of conservation equations is complete after the description of initial and boundary conditions.

3.2 Numerical Methodology

The governing equations described in Sec. 3.1 are solved using a well-established three-dimensional parallel, multi-species compressible flow solver, referred to as AVF-LESLIE [18, 37]. It is a multi-physics simulation tool capable of DNS and LES of reacting/non-reacting flows in canonical and moderately complex flow configurations. It has been extensively used in the past to study a wide variety of flow conditions, including acoustic flame-vortex

interaction, premixed flame turbulence interaction, scalar mixing, non-premixed combustion, etc. [18, 37, 56, 57]. The solver utilizes a finite volume-based spatial discretization of the governing equations in their conservative form on a structured grid using the generalized curvilinear coordinates. The spatial discretization is based on the well-known 2nd/4th-order accurate MacCormack scheme [26]. The time integration of the semi-discrete system of equations is performed by an explicit 2nd-order accurate scheme. The solver can handle arbitrarily complex finite-rate chemical kinetics. The mixture-averaged transport properties, the finite-rate kinetics source terms, and the thermally perfect gas-based thermodynamic properties are obtained using the Cantera software [17].

To assess the effects of the complexity of chemical mechanisms on the turbulence-chemistry interactions while employing finite-rate chemical kinetics, we consider two different chemical mechanisms. These include a moderately complex 8-species and 4-step mechanism [41], and a skeletal 13-species and 73-step mechanism [36]. The species in the first mechanism include CH_4, O_2, CO, CO_2, H, H_2, H_2O, N_2, and the species in the second mechanism include CH_4, CH_3, CO, CO_2, CH_2O, O, O_2, H, H_2, OH, H_2O HO_2, N_2.

CHAPTER 4

DESCRIPTION OF COMPUTATIONAL SETUP AND CASES

In this chapter, the details of the computational setup and cases considered in this study are discussed. These details include the computational domain, computational mesh, the initial/boundary conditions, a description of the cases, and the simulation parameters.

4.1 Computational Setup

Figure 4.1 (a) shows a schematic of the turbulent premixed flame configuration. We consider four different methane/air turbulent premixed flames in this study to analyze the effects of pressure and chemical models while employing the finite-rate chemistry approach on the turbulence-chemistry interactions. These flames correspond to the TRZ and the B/DRZ reaction zone regimes (based on the initial turbulence and flame conditions). The four cases considered here are shown on the premixed regime diagram [30] in Figure 4.1 (b). In this figure, the symbols (●), (■), (▲), and (◆), correspond to cases A1, A2, A3, and A4, respectively.

The computational domain is 3-dimensional with dimensions of $L_x \times L_y \times L_z$ in the streamwise (x), transverse (y) and spanwise (z) directions. Hereafter, $(x_1,\ x_2,\ x_3) \equiv (x,\ y,\ z)$, and they are used interchangeably. The flow field is initialized using an isotropic turbulent flow field obtained using the Kraichnan spectrum [21]. The value of L is chosen so

that it is at least 10 times the integral length scale l_t of the initial isotropic turbulence. The background turbulent flow field is superimposed with the one-dimensional planar laminar premixed flame solution obtained at $\phi = 0.8$, $T_{\text{ref}} = 570$ K and $p_{\text{ref}} = 1$ atm or 10 atm.

The flame conditions, particularly the preheated conditions and the equivalence ratio, chosen here are nominally based on past studies and are typical of gas turbines, spark-ignition engines and combustors [35, 37]. The center of the initially planar laminar premixed flame is positioned near the center of the computational domain with the reactants on the left and the products on the right sides (see Figure 4.1 (a)). A characteristic-based inflow-outflow boundary condition is used in the x direction and periodic boundary conditions are used in the homogeneous y and z directions.

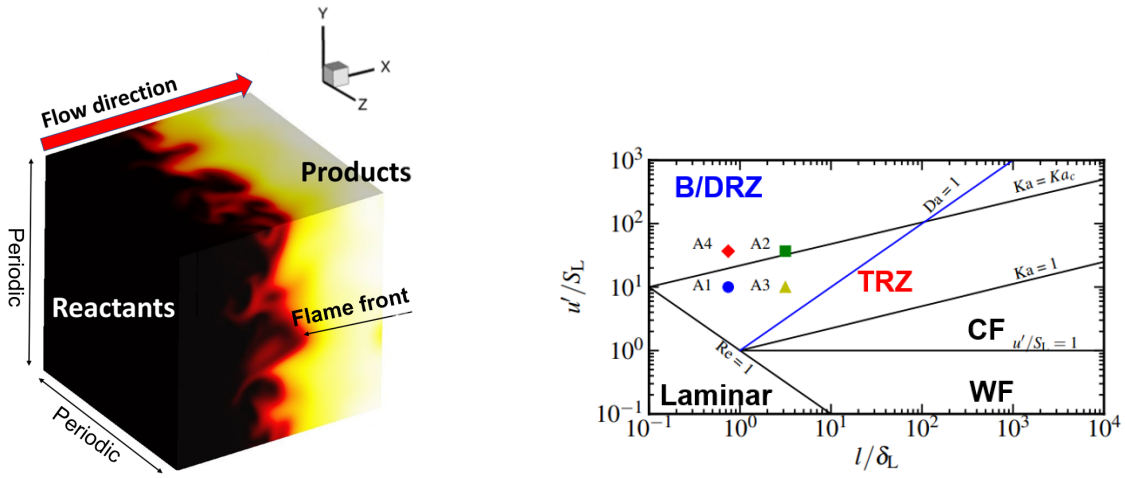

(a) (b)

Figure 4.1 A schematic of the turbulent premixed flame configuration (a) and the premixed regime diagram [30] (b) for the cases investigated in this study

4.2 Description of Cases

The four cases considered in this study correspond to the TRZ and B/DRZ regimes (see Figure 4.1 (b)) based on the initial flame and turbulence conditions. These cases are characterized on the regime diagram in terms of the characteristic velocity scale ratio (u'/S_{L}) and the characteristic length scale ratio (l_t/δ_{L}). Here, u' and l_t denote the turbulence intensity and the integral length scale of the initial turbulence, and S_{L} and δ_{L} denote the laminar flame speed and laminar thermal flame thickness of the initially planar premixed flame. Furthermore, the cases can be characterized in terms of other non-dimensional parameters, such as the integral Reynolds number (Re), the Karlovitz number (Ka), and the Damköhler number (Da), which are defined as

$$Re = \frac{u' l_t}{\nu}, \tag{4.2.1}$$

$$Ka = \sqrt{\frac{u'^3 \delta_{\mathrm{L}}}{S_{\mathrm{L}}^3}}, \tag{4.2.2}$$

$$Da = \frac{S_{\mathrm{L}} l_t}{u' \delta_{\mathrm{L}}}. \tag{4.2.3}$$

Note that the laminar thermal flame thickness δ_{L} is defined as

$$\delta_{\mathrm{L}} = \frac{(T_{\mathrm{b}} - T_{\mathrm{u}})}{|\nabla T|_{\max}}, \tag{4.2.4}$$

where, the subscripts 'b' and 'u' denote burnt and unburnt regions, respectively.

Table 4.1 Simulation parameters

Case	Closure	$N_x \times N_y \times N_z$	p_{ref} [atm]	u'/S_L	l_t/δ_L	Re	Ka	Da
A1	DNS	$256 \times 256 \times 256$	1	10.0	0.74	61.6	12.7	0.62
A2	DNS	$512 \times 512 \times 512$	10	36.8	3.15	621	54.4	0.46
A3	DNS	$384 \times 384 \times 384$	10	10.0	3.15	168	7.7	1.68
A4	DNS	$256 \times 256 \times 256$	10	36.8	0.74	146	111.9	0.11

The simulation parameters for the four cases are summarized in Table 4.1. These cases are labeled A1, A2, A3, and A4. Specifically, cases A1 and A3 correspond to the TRZ regime with Ka of about 13 and 8, respectively, whereas cases A2 and A4 fall within the B/DRZ regime with Ka of about 54 and 112. The four cases are considered to characterize the effects of pressure, effects of variation in u'/S_L for fixed l_t/δ_L, and the effects of variation in l_t/δ_L for a fixed u'/S_L. Note that an increase in pressure causes the laminar flame speed and the laminar thermal flame thickness to decrease, so to evaluate the effects of pressure, Case A2 is simulated at 10 atm while maintaining the same initial background turbulence conditions, i.e., the same integral length scale, l_t, and the turbulence intensity, u' as Case A1. To evaluate the effects of change in l_t/δ_L due to change in pressure, Case A3 is simulated at 10 atm while keeping u'/S_L to be the same as Case A1. To evaluate the effects of changes in u'/S_L due to the change in the pressure, Case A4 is simulated at 10 atm while maintaining l_t/δ_L to be the same as Case A1.

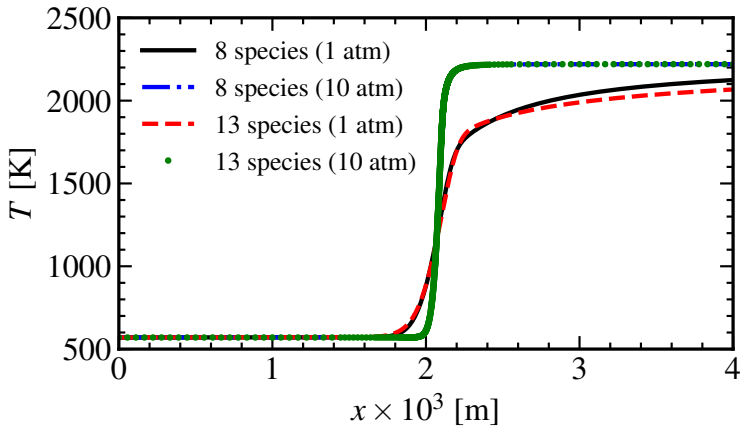

Figure 4.2 Spatial variation of temperature for the laminar premixed flame using two chemical mechanisms at pressure of 1 atm and 10 atm

The four cases considered in this study are simulated using two different chemical mechanisms to examine the effects of the complexity of finite-rate chemistry models on the features of the turbulent premixed flames. These mechanisms include a moderately complex 8-species and 4-step mechanism [41], and a skeletal 13-species and 73-step mechanism [36]. Therefore, a total of eight simulations are conducted in the present study. The differences in the properties of the laminar premixed flame and the adiabatic flame temperature obtained using the two chemical models employed in this study are summarized in Table 4.2. The 8-species mechanism yields higher value of S_{L} at $p_{\mathrm{ref}} = 1$ atm compared to the 13-species mechanism. However, at $p_{\mathrm{ref}} = 10$ atm, both the mechanisms yield similar values of S_{L}, which as expected, is reduced compared to the atmospheric pressure flame. The value of δ_{L} from the two chemical models do not show noticeable differences. The adiabatic flame temperature (T_{ad}) as expected is higher in the 8-species mechanism due to a lack of some of the other intermediate species, which are present in the 13-species mechanism.

The spatial variation of the temperature field obtained using the two chemical mech-

Table 4.2 Properties of laminar premixed flame and adiabatic flame temperature for different cases at $T_{\text{ref}} = 570$ K and $\phi = 0.8$.

Case	Mechanism	p_{ref} [atm]	S_{L} [m/s]	$\delta_{\text{L}} \times 10^3$ [m]	T_{ad} [K]
Case A1	8-species	1	1.24	0.33	2200
	13-species	1	0.98	0.34	2182
Case A2	8-species	10	0.33	0.08	2214
	13-species	10	0.36	0.07	2202
Case A3	8-species	10	0.33	0.08	2214
	13-species	10	0.36	0.07	2202
Case A4	8-species	10	0.33	0.08	2214
	13-species	10	0.36	0.07	2202

anisms at $p_{\text{ref}} = 1$ atm and 10 atm is shown in Fig. 4.2. The temperature profile shows some sensitivity to the employed chemical mechanism at 1 atm. However, at 10 atm, both the mechanisms yield nearly the same temperature field. Therefore, the behavior of the turbulent premixed flames considered in this study under these conditions, particularly at elevated pressure, will be related to the highly nonlinear turbulence-chemistry interactions.

The computational domain is spatially discretized using a grid resolution of N_x, N_y and N_z along x-, y- and z-directions, respectively. The grid resolution is chosen based on the past studies [34], and for the conditions reported here is sufficient to reach $k_{\max}\eta \geq 1$ in all cases, where $k_{\max}$ is the largest wave number and η is the Kolmogorov length scale. Additionally, the flame structure is adequately resolved to ensure approximately 10 points or more across the thermal flame thickness [6] in all cases.

The simulations are carried out long enough to allow for the evolution of flame-turbulence interactions. All the results are examined after two initial eddy turnover times, i.e., $t/t_0 = 2$. Here, $t_0 = l_t/u'$, which denotes the initial eddy turnover time. Even though turbulence decays in time in the present study, there is a period during which flame-turbulence interaction attains a quasi-stationary state, and therefore, the dynamics and statistics associated with the flame-turbulence interaction can be analyzed during such period. Typically, the initialization with the Kraichnan spectrum evolves to a physical state in about one eddy turnover time, therefore two eddy turnover times are adequate enough for flame-turbulence interaction to evolve [39] so that the statistical features of the flames can be analyzed.

CHAPTER 5

EFFECTS OF ELEVATED PRESSURE

This chapter presents the results from the DNS of the turbulent premixed flame cases and discusses the effects of elevated pressure. First, the flame structure and wrinkling are qualitatively discussed in Sec 5.1, and then the spatially averaged statistics are presented in Sec. 5.2. Next, the effects of elevated pressure on the conditional statistics are discussed in Sec. 5.3. Afterward, the statistics of flame curvature and HRR are described in Sec. 5.4. Finally, in Sec. 5.5, the spectral characteristics are discussed in terms of the spectral kinetic energy (SKE) and the SKE transport terms (non-linear advection, pressure gradient, viscous diffusion, and dilatational effects). The results in this chapter are based on the simulations employing the moderately complex 4-step and 8-species chemical mechanism [41]. The results are analyzed after two eddy turnover times, i.e., $t/t_0 = 2$.

5.1 Structural Features of Flow and Flame

The flame topology and behavior are highly sensitive to the effects of an increase in pressure. This section qualitatively discusses these effects by examining the structural characteristics in terms of the contours in the central slices ($x_1 - x_2$ plane) of progress variable (c), temperature (T), and vorticity magnitude ($||\boldsymbol{\omega}||$). The fuel mass fraction based progress variable, c is defined as

$$c = \frac{Y_{\mathrm{CH_4}} - Y_{\mathrm{CH_4,u}}}{Y_{\mathrm{CH_4,b}} - Y_{\mathrm{CH_4,u}}}, \tag{5.1.1}$$

where, 'u' and 'b' denote the unburnt reactants and burnt products sides, respectively. Here, $c \in [0,\ 1]$ with $c = 0$ corresponding to the reactants and $c = 1$ corresponding to the products sides.

The contours of c are shown in Fig. 5.1. In these figures, the streamwise (x) axis have been made dimensionless and are denoted by $(x_i - x_0)/L$. Here, $i = 1, 2, 3$ correspond to the Cartesian grid coordinates, and x_0 is the mean global flame position, which is defined as

$$x_0(t) = \frac{1}{L^2 \left(\rho Y_{CH_4}\right)_{\mathrm{u}}} \int_{\Omega} \rho Y_{CH_4} dV, \tag{5.1.2}$$

where, Ω denotes the computational domain.

In Fig. 5.1, the solid, black curve near the center of the domain indicates the nominal location of the instantaneous flame front defined by the iso-value of the progress variable, i.e., $c = 0.8$. In Case A1, the flame-turbulence interaction leads to distortion of the initially planar flame front. The contours show mixing of partially burnt and unburnt fluid ahead of the reaction zone ($(x_1 - x_0)/L \lessapprox 0$). Furthermore, the transport of mass and heat is enhanced, which causes homogenization within the flame brush leading to a decrease in the gradient of the progress variable. Such behavior of premixed flames in the TRZ regime has also been observed in past studies [29, 34, 37].

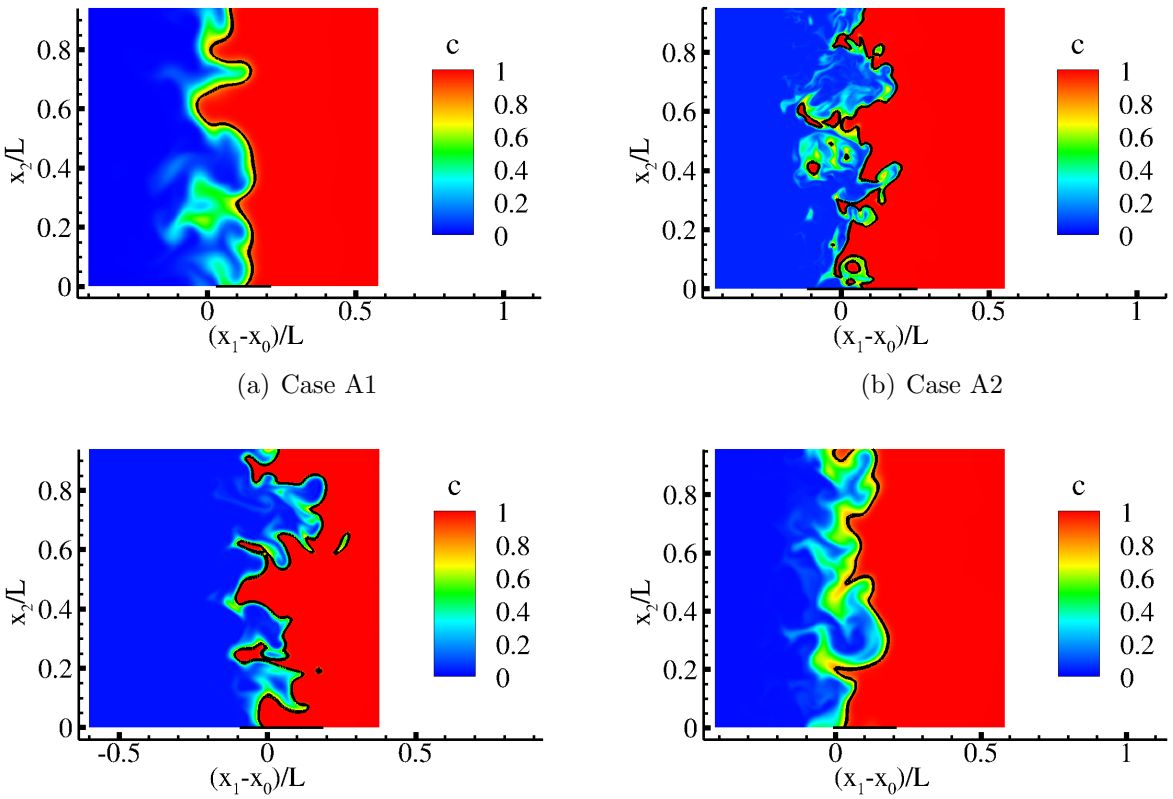

(a) Case A1

(b) Case A2

(c) Case A3

(d) Case A4

Figure 5.1 Instantaneous contours of the progress variable, c, in the central $x_1 - x_2$ plane at $t/t_0 = 2$

Increasing the pressure while keeping the background turbulence characteristics the same, as in Case A2, leads to much finer distortion of the flame front by the turbulent eddies, which has also been reported in the study by Wang et al. [52]. Additionally, there is a decrease in the flame thickness and flame speed, a less defined flame front, and pockets of completely burnt reactants in the reaction zone as seen in Fig. 5.1 (b), which implies a severe disruption of the flame structure. The effects of pressure are clearly evident in Case A2 compared to Case A1, where a continuous reaction layer is evident. Note that due to increased pressure with the turbulence characteristics being the same, Case A2 corresponds to the B/DRZ regime compared to Case A1, which corresponds to the TRZ regime. Therefore, turbulent eddies significantly affect the flame structure in Case A2, which is similar to the observations in the past studies of turbulent premixed flames under extreme turbulent environment [2, 24, 38, 42, 48, 49].

Increased pressure while maintaining a constant velocity scale ratio (u'/S_{L}), as in case A3, also leads to severely perturbed flame structure and a thinner flame brush thickness. However, the flame front is less disturbed than in Case A2 because this case still corresponds to the TRZ regime, where turbulent eddies are not energetic enough to cause severe distortion to the flame structure. Such behavior has also been observed by Klein et al. [19] where it was reported that for a given pressure, decreasing the velocity scale ratio results in less wrinkling. Additionally, Fig. 5.1 (c) shows that maintaining a constant u'/S_{L} shifts the location of the instantaneous flame front further downstream, which was previously reported in both computational and experimental results [58].

Finally, maintaining a constant length scale ratio (l_t/δ_{L}) while increasing pressure leads to a more stable and less wrinkled flame structure than cases A2 and A3. Klein et al. [19] came to similar conclusions in their DNS analysis of Bunsen flames and reported that at elevated pressures, decreasing the integral length scale resulted in less instability of the flame structure. The preheat zone of Case A4 is broader than the other cases, which results in a thicker flame brush. This is likely caused by turbulence-flame interactions generating smaller-scale eddies that enhance heat and mass transport and homogenization within the flame brush region.

Figure 5.2 shows the contours of the normalized temperature, where the adiabatic flame temperature (T_{ad}) is used to perform the normalization. The temperature variation around the flame front draws similar conclusions as the variation of the progress variable. The case at atmospheric pressure, i.e., Case A1, is shown in Fig. 5.2 (a) and displays a smooth temperature gradient around the reaction zone, typical of flames at atmospheric pressure in the TRZ regime [37]. Cases A2 and A3 display much sharper temperature gradients, whereas Case A4 displays a similar temperature gradient to Case A1 with slightly more perturbations to the continuous flame front. The flame brush thickening causes a broader temperature distribution in Case A4 due to homogenization of the flame brush resulting from the enhanced heat and mass transport. Qualitatively, the variation of c and T shown in Figs. 5.1 and 5.2, respectively, indicates a correlation of these quantities for the cases considered here, which will be discussed later quantitatively.

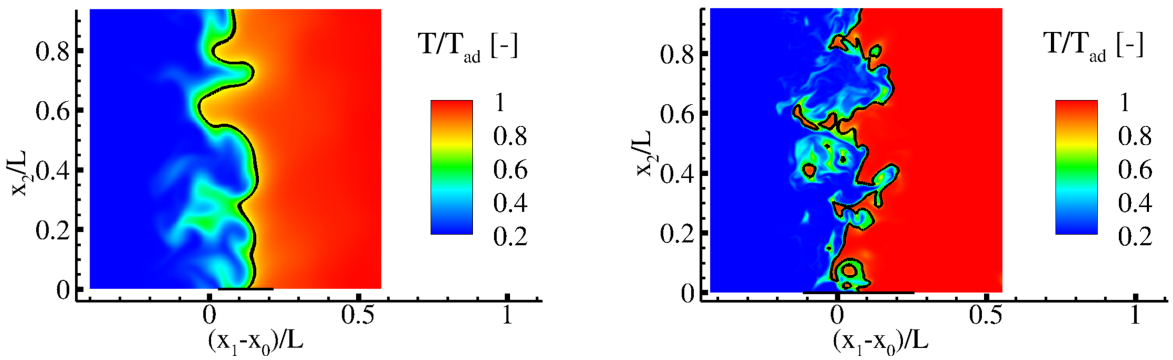

(a) Case A1 (b) Case A2

(c) Case A3 (d) Case A4

Figure 5.2 Instantaneous contours of the normalized temperature, (T/T_{ad}), in the central $x_1 - x_2$ plane at $t/t_0 = 2$

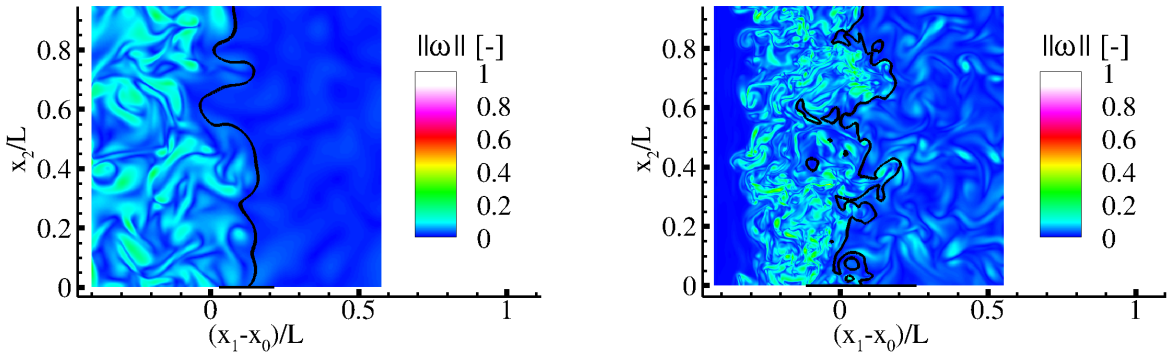

(a) Case A1

(b) Case A2

(c) Case A3

(d) Case A4

Figure 5.3 Instantaneous contours of vorticity magnitude in the central $x_1 - x_2$ plane at $t/t_0 = 2$

The effects of the presence of flame on the background turbulence are evident from the contours of the instantaneous $||\boldsymbol{\omega}||$ shown in Fig. 5.3. Here, $||\boldsymbol{\omega}||$ is non-dimensionalized by the corresponding peak value for each case. Due to an increase in the viscosity in the product region resulting from an increase in the temperature, the small-scale structures tend to disappear in all of the cases. The rise in pressure in Case A2 causes sharper and more intense vorticity gradients than Case A1. Figure 5.3 (a) shows how Case A1 is characterized by small-scale turbulent structures that do not penetrate past the flame front. Cases A2 and A3 have some small-scale structures behind the flame front, penetrating the reaction zone and continuing into the post-flame zone. In Case A4, the flow structures are very similar to Case A1, and similarly, these structures do not penetrate the innermost layer of the flame. It is evident from Fig. 5.3 that elevated pressure causes significant flame front wrinkling. For flames in the B/DRZ regimes, reducing the integral length scale to maintain a constant length scale ratio, leads to a reduced wrinkling.

Overall, the results of the instantaneous flame and flow structures discussed in this section highlight the highly nonlinear nature of flame-turbulence interactions. Furthermore, the effects of an increase in pressure with fixed background turbulence characteristics, fixed velocity scale ratio, and fixed-length scale ratio further illustrates changes to the characteristic features of turbulent premixed flames. A quantitative description of such interactions is discussed next.

5.2 Spatially Averaged Statistics

In this section, the spatially averaged statistics of the different cases are examined. The spatially averaged statistics are obtained by averaging along the homogeneous x_2 (y)- and x_3 (z)-directions through

$$\langle q \rangle (x,t) \equiv \frac{1}{L^2} \int_0^L \int_0^L q(x,y,z)\, dy\, dz, \tag{5.2.1}$$

where, q denotes any field variable such as temperature, mass fraction of species, progress variable, etc.

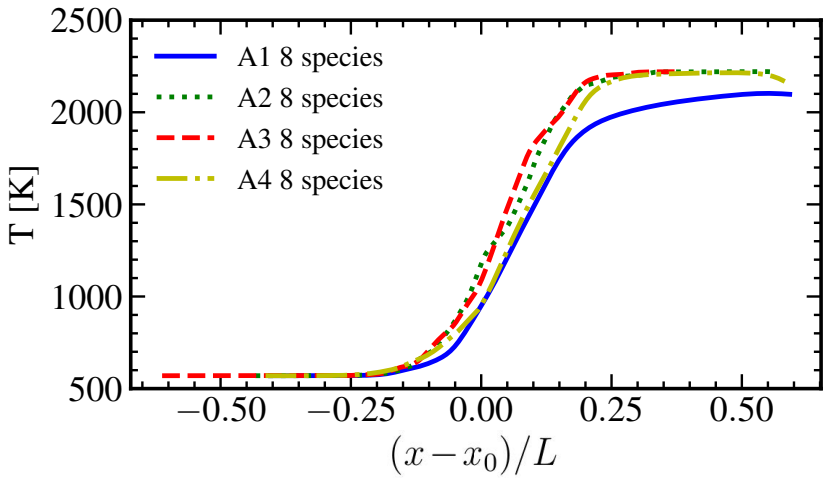

Figure 5.4 Spatially averaged profile of the temperature field

Figure 5.4 compares the spatial variation of the average temperature at $t/t_0 = 2$ for all four cases. As expected, all the high-pressure cases reach higher maximum temperatures than the atmospheric pressure case due to a higher T_{ad} (see Table 4.2). The gradient of the temperature field in the different cases provides further insight into the behavior of the

flame at elevated pressures. In particular, the initial change in the temperature for the high-pressure cases is steeper than that of Case A1. After this initial temperature change, the slope for Case A4 is almost entirely the same as Case A1 despite the distribution being slightly broader. The broader profile observed in Case A4 compared to Case A1 is due to the enhanced homogenization effect of the turbulent eddies. Conversely, the slopes for cases A2 and A3 are steeper and narrower than case A4, which corresponds to the thinner flame thicknesses observed for these cases in Fig. 5.4, and can be attributed to the effect of the high-pressure conditions. These variations in the gradient of the temperature distribution correspond to the variations seen in the contours of the temperature field in Fig. 5.2.

Additionally, temperature distributions for cases A1 and A4 display the same linear behavior along the flame front, but cases A2 and A3 have variations in their slopes. For instance, in Case A2, the temperature is increasing very sharply until around the mean global flame position, where there is a sudden decrease in the rate of temperature change. Case A3 exhibits a similar variation.

The behavior of the temperature distribution in the post-flame is also intriguing. In the high-pressure cases, it is observed that the maximum temperature is reached very quickly, and this temperature is sustained for the remainder of the computational domain due to a completion of combustion of the fuel. In contrast, in Case A1, the temperature increases gradually, and the maximum temperature is only observed towards the end of the computational domain.

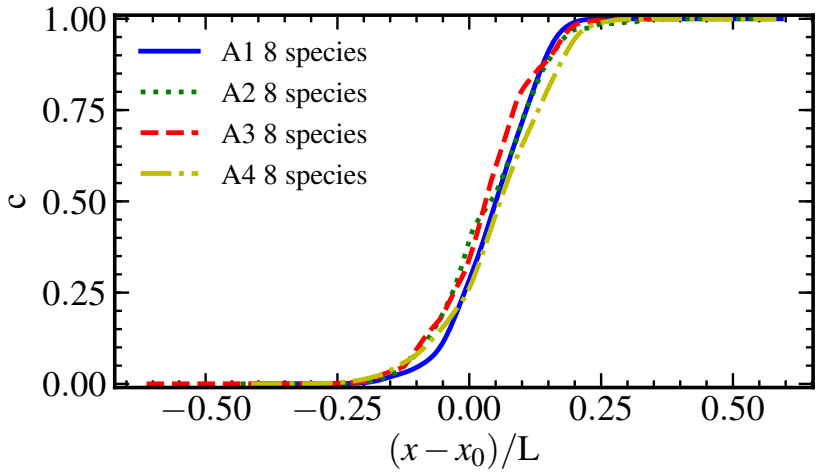

Figure 5.5 Spatially averaged profile of the progress variable, c

Similar behavior is also observed in the spatial variation of the average progress variable shown in Fig. 5.5. There are changes in the slopes of the progress variable distribution for cases A2 and A3 that correspond to the exact location as the fluctuations in their temperature profiles in Fig. 5.4. This further emphasizes the correlation between the progress variable and the temperature field in the high-pressure cases, which is discussed further in Sec. 5.3. Additionally, the spatial variation of the progress variable observed for Case A4 is less steep and broader than Case A1 due to enhanced homogenization effects within the preheat zone of the flame brush.

The spatial variation of the averaged mass fraction of the intermediate species, namely, CO and H_2 are shown in Fig. 5.6. In the high-pressure cases, CO is completely oxidized into CO_2 in the post-flame zone. However, CO is a product of combustion for the case at atmospheric pressure. Note that CO requires exceedingly high temperatures to oxidize, and then it oxidizes at a slower rate. The presence of the CO emissions in Case A1 is likely a result

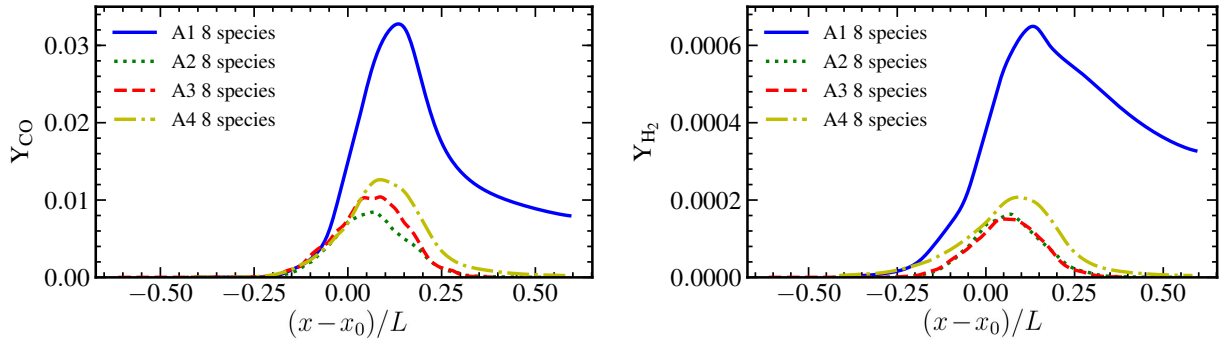

(a) Mass fraction of CO

(b) Mass fraction of H_2

Figure 5.6 Spatially averaged profile of mass fraction of the intermediate species

of the temperature increasing too slowly in the post-flame region, as seen in Fig. 5.4. The temperature of Case A1 rises gradually and does not reach the maximum flame temperature until late in the post-flame zone. In contrast, the high-pressure cases reach and maintain the maximum flame temperature early in the post-flame zone, and as a result, CO is completely oxidized. Similar behavior is also observed in the spatial variation of the mass fraction of H_2, again indicating the effects of operating pressure on the intermediate species.

5.3 Statistical Features of Flame-Turbulence Interaction

To further examine the effects of pressure on flame-turbulence interactions in the state-space, the variation of the fuel reaction rate, $\dot{\omega}_{CH_4}$, mass fractions of the intermediate species, and temperature with respect to the progress variable, c, is examined in this section.

The conditional variation of $\dot{\omega}_{CH_4}$ with respect to c is shown in Fig. 5.7. It is evident that the reaction rate distributions are steeper in the high-pressure cases, and the magnitudes of the peak reaction rate are much higher than the case at the atmospheric pressure. In Case A4, $\dot{\omega}_{CH_4}$ reaches its maximum magnitude at about $c = 0.96$, whereas cases A2 and A3 reach

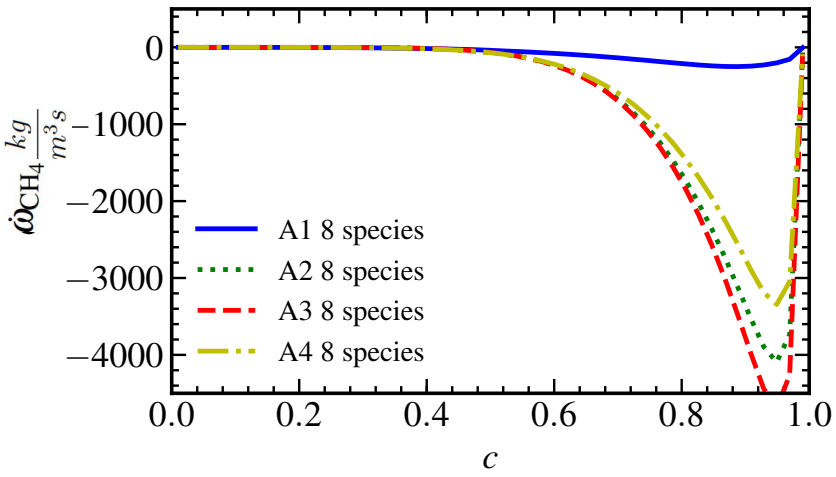

Figure 5.7 Reaction rate of methane conditionally averaged with respect to the progress variable

their maximum reaction rate at about $c = 0.94$. The distribution of the reaction rate for Case A1 has a maximum reaction rate magnitude of only about $200\frac{\text{kg}}{\text{m}_3\text{s}}$. Case A3 has the highest reaction rate magnitude of about $4500\frac{\text{kg}}{\text{m}^3\text{s}}$, Case A2 reaches a maximum reaction rate magnitude of about $4100\frac{\text{kg}}{\text{m}^3\text{s}}$, and Case A4 reaches a maximum reaction rate magnitude of about $3400\frac{\text{kg}}{\text{m}^3\text{s}}$. Apart from the magnitude of the reaction rate, the reaction rate variation is much sharper in the high-pressure cases, which is consistent with the thin reaction layers evident in Figs. 5.1 and 5.2.

The variation of the mass fractions of the intermediate species, specifically, CO and H_2 with respect to the progress variable, is shown in Fig. 5.8. The total mass fractions of CO and H_2 for Case A4 are lower than the other cases, where the case at atmospheric pressure has significantly higher values of CO and H_2 in the post-flame region. As discussed in Sec. 5.2, with Figs. 5.4 and 5.6, the lower peak temperature and the slower increase in temperature in the post-flame region can attribute to higher values of CO for Case A1. For

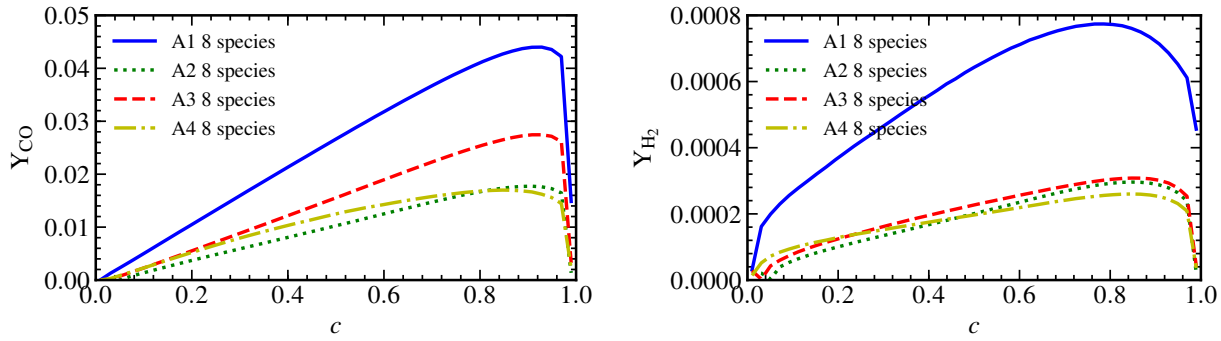

(a) Mass fraction of CO

(b) Mass fraction of H_2

Figure 5.8 Mass fraction of the intermediate species conditionally averaged with respect to the progress variable

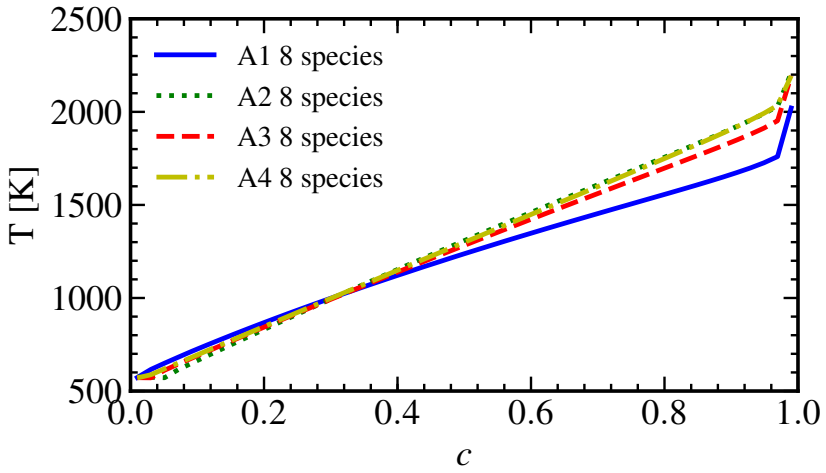

Figure 5.9 Temperature field conditionally averaged with respect to the progress variable

the mass fraction of CO, the distribution is nearly linear for cases A1, A2, and A3. Case A4 presents a different distribution behavior like Case A3 until around $c = 0.28$, at which point the slope significantly decreases, resulting in a flatter curve. The variation of H_2 mass fraction with respect to c shows an evident effect of pressure like the variation of the CO mass fraction.

Figure 5.9 shows the conditional variation of temperature with respect to the progress variable. In all cases, a quasi-linear variation is evident, particularly in the preheat zone, indicating a highly positive correlation of these two quantities, which was also observed in Figs. 5.1 and 5.2. This correlation is higher in high-pressure cases. Furthermore, in all four cases, the maximum temperature occurs between about $c = 0.96 - 1.00$.

For cases A2, A3, and A4, the temperature increases linearly with the progress variable. However, for Case A1, the temperature rise is nonlinear, and its slope is less steep, particularly in the post-flame region, which corresponds to the slow temperature increase observed in this region in Fig. 5.4. These results indicate that the progress variable is correlated to the temperature field for the cases considered in the present study.

5.4 Curvature and Heat Release Rate Statistics

The coupling of differential diffusion (non-unity Lewis number) effects with the flame curvature κ significantly impacts the local burning rate of a flame. The flame curvature is defined as

$$\kappa = \nabla \cdot \mathbf{n}, \tag{5.4.1}$$

where, $\mathbf{n}$ is the unit normal vector of the flame front given by $\mathbf{n} = \dfrac{-\nabla c}{|\nabla c|}$. When curvature is positive (negative), this means that it is convex (concave) towards the reactants. The role of curvature on the flame propagation and the burning rate has been studied extensively in the past for premixed flames under different flow conditions [14, 28, 35, 37, 46, 59].

For example, in the case of $Le < 1$, the diffusion of reactants is higher than the thermal diffusion. Therefore, regions of flame having a convex/concave shape towards reactants leads to a focusing/de-focusing effect, which increases/decreases the local reaction rate and the flame propagation speed.

The measures of central tendency can provide important insight into the curvature characteristics and are outlined in Table 5.1. Here, μ, σ ,and γ denote the mean, standard deviation, and the skewness. The standard deviation, σ, describes the width of the probability density function (PDF). A higher value of σ indicates a broader PDF and a higher probability for large curvature. The probability density function of the flame curvature is computed at the instantaneous flame front for all the cases presented in Figure 5.10. Here, the instantaneous flame front is defined by the progress variable at $c = 0.8 \pm 0.125$, and κ is scaled using δ_{L} following the past study [55].

Table 5.1 Measures of central tendency for the flame curvature

Case	μ	σ	γ
A1	0.47	2.82	1.33
A2	0.53	3.62	0.79
A3	0.12	1.50	0.21
A4	1.11	5.29	1.78

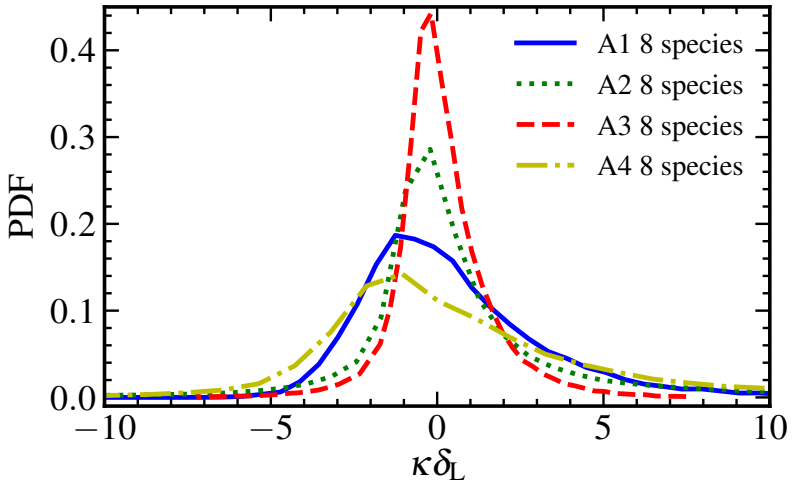

Figure 5.10 Probability density function (PDF) of the flame curvature at the instantaneous flame front

The case at atmospheric pressure is positively skewed with a mean of $\mu = 0.47$ and skewness of $\gamma = 1.33$. Increasing pressure while keeping l_t and u' constant, as in Case A2, causes the PDF of κ to become less positively skewed with $\gamma = 0.79$. When pressure is increased while maintaining a constant u'/S_L, as in Case A3, the PDF becomes narrower, skewness decreases to 0.21, and the distribution is nearly symmetrical, which is in agreement with the results reported by Klein et al. [19]. Case A4 is at an elevated pressure while maintaining a constant l_t/δ_L, and in this case, the distribution becomes flatter, broader, and more skewed with $\gamma = 1.78$. The broadening of the PDF indicates a higher probability of a large magnitude of curvature. Comparing the high-pressure cases only, it is clear that the degree of skewness and likelihood for large values of κ increases with increasing Karlovitz number. This trend is also observed in the study by Wang and Abraham [55].

In Figure 5.11, the non-dimensional HRR conditionally averaged on the progress variable is shown for all cases. In this figure, it is evident that elevated pressure affects the

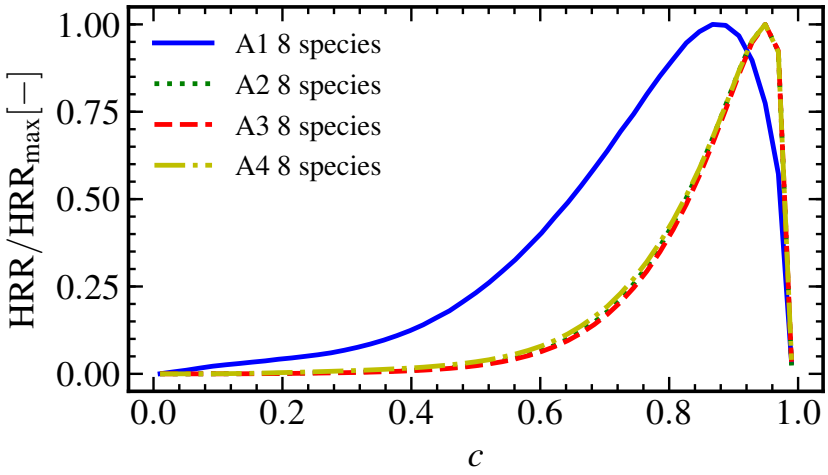

Figure 5.11 Conditional variation of HRR with respect to the progress variable

behavior of the maximum HRR. The distributions in the high-pressure cases are incredibly similar and collapse on each other. The HRR distribution is steeper for the high-pressure cases, and the maximum HRR for these cases occurs at about $c = 0.94$. In contrast, the maximum HRR for Case A1 occurs at about $c = 0.86$, demonstrating a shift in the peak burning towards higher temperature. These results indicate that the effect of elevated pressure on peak burning is more significant than the effects of variation in the u'/S_{L} and l_t/δ_{L}.

The variation of HRR with respect to κ is now examined by plotting the HRR against the normalized flame curvature at the flame front, which is shown in Fig. 5.12. Here, κ is computed at the instantaneous flame front define as, $c = 0.8 \pm 0.125$ and normalized by the thermal flame thickness δ_{L}. It is clear that all cases have a moderate yet negative correlation between HRR and κ, and HRR is biased to positive values of κ in the high-pressure cases. However, the behavior of this correlation varies in each case. For example, the case at atmospheric pressure displays a stronger correlation in the negative regions.

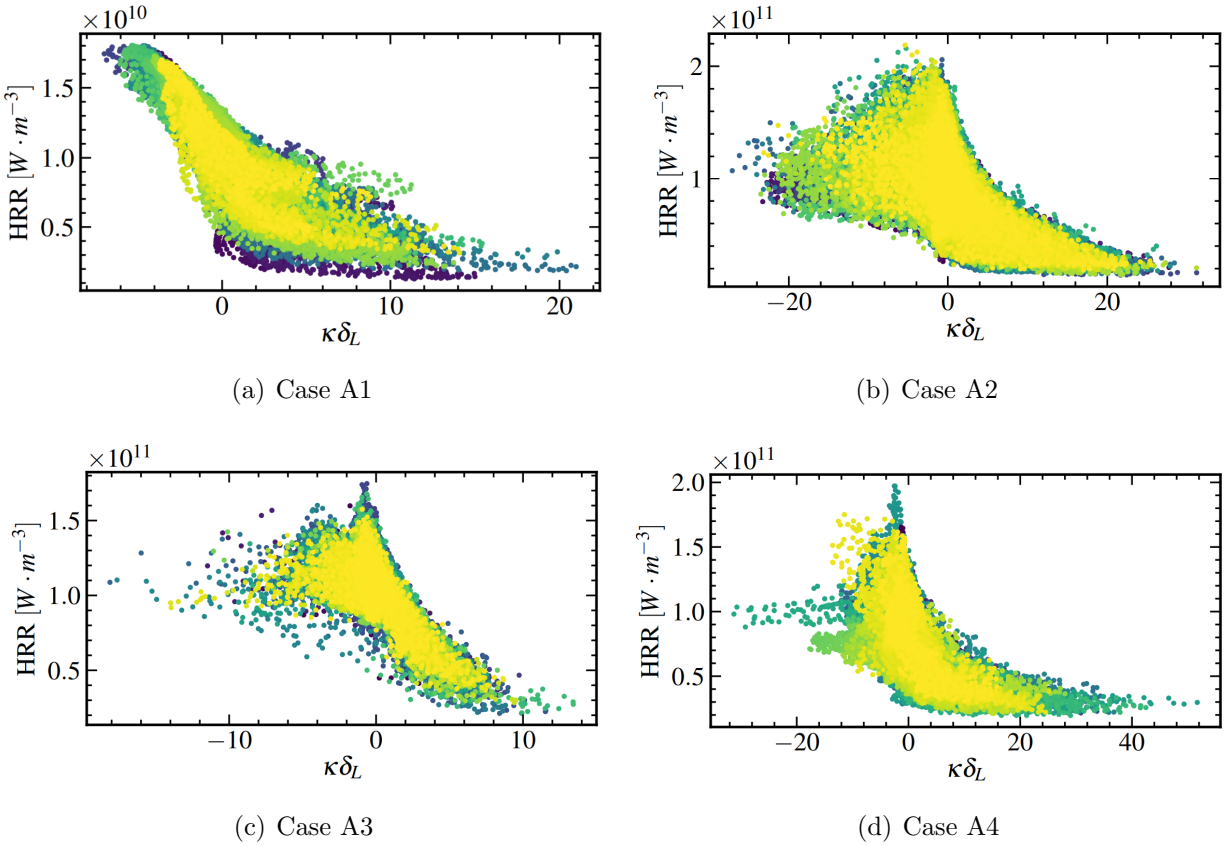

(a) Case A1

(b) Case A2

(c) Case A3

(d) Case A4

Figure 5.12 Scatter of HRR with respect to the flame curvature

On the other hand, when pressure is increased with a constant value of l_t and u', as in Case A2, there is a stronger correlation in the positive curvature regions and an increase in scattering occurs in the negative curvature regions. Increasing pressure with a constant value of u'/S_{L} presents similar results. When pressure is increased with a constant value of l_t/δ_{L}, as in Case A4, there is less scatter in the negative curvature regions when compared to cases A2 and A3. For cases A3 and A4 the maximum HRR values occur near $\kappa\delta_L = 0$. However, for Case A2, the maximum HRR values occur to the left of $\kappa\delta_L = 0$, and they occur even farther for the case at atmospheric pressure at about $\kappa\delta_L = -7$. This change in maximum HRR behavior indicates that at elevated pressure, the maximum HRR values

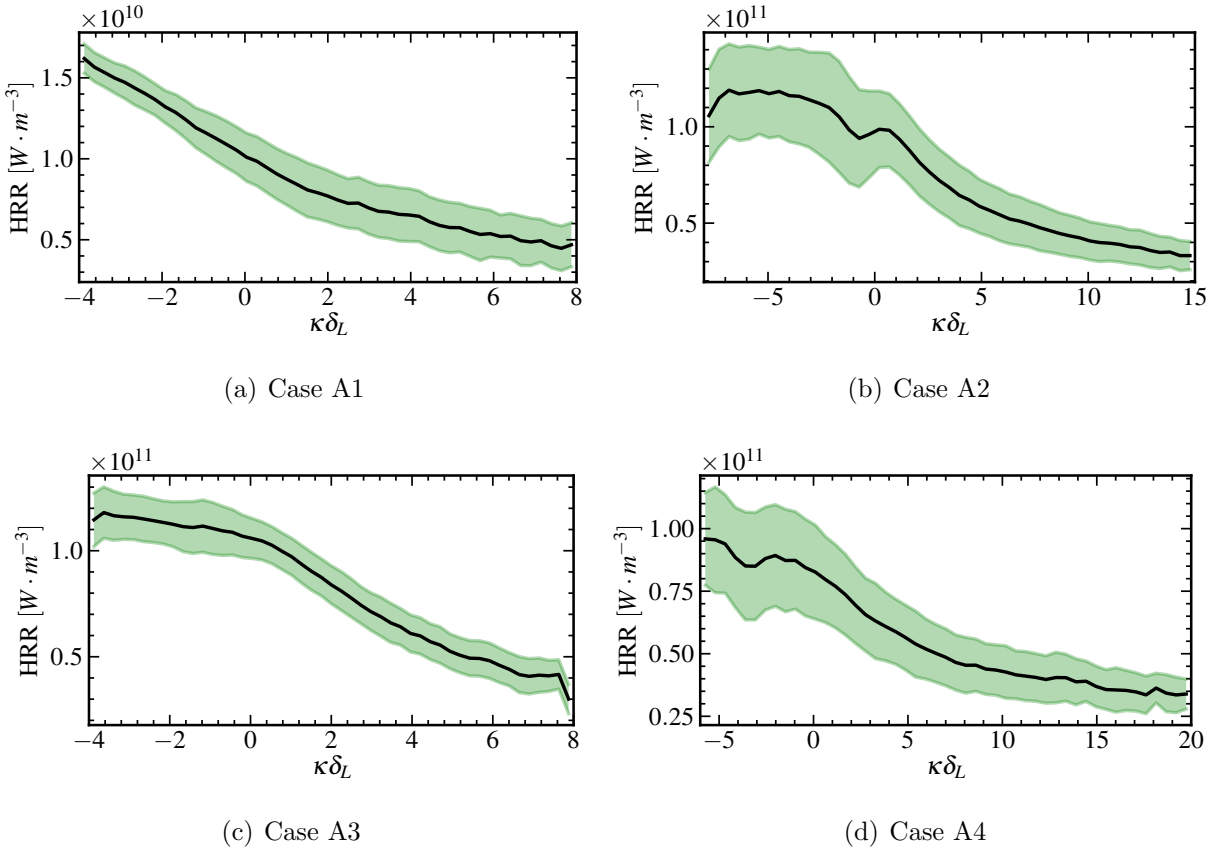

(a) Case A1

(b) Case A2

(c) Case A3

(d) Case A4

Figure 5.13 HRR conditioned on curvature with descriptive statistics

are not occurring in the regions of highest negative curvature but rather near these regions. Dinesh et al. [8] reported the same observations for HRR and referred to the areas where maximum HRR is occurring as "flank regions."

The differences in the relationships between HRR and curvature are even more apparent when the HRR is conditionally averaged on the flame curvature. Figure 5.13 shows the conditionally averaged HRR with respect to κ where the green regions are $\pm$ one standard deviation away from the averaged HRR. The variation of HRR with κ is nearly monotonically decreasing for all cases. However, there are significant differences between the four

cases when one examines the standard deviation of HRR. Compared to cases A2 and A4, the standard deviation of HRR is small for cases A1 and A3.

Furthermore, the standard deviation is the largest in the positive curvature regions and smallest in the negative curvature regions for the case at atmospheric pressure. In contrast, the high-pressure cases display the opposite behavior, with standard deviation being the largest and smallest in the negative and positive curvature regions, respectively. It is evident from Figs. 5.10-5.13 that increasing pressure has a significant effect on flame curvature, HRR, and their relationship.

5.5 Comparison of Spectral Characteristics

Spectral analysis can provide insight into how various length scales contribute to the transfer of kinetic energy. Two-dimensional spectral kinetic energy (SKE) of the turbulent premixed flames are computed by performing a Fourier transform of the three-dimensional reacting flow field. Following the approach described in [45], we investigate the roles of individual terms in the compressible Navier-Stokes equation, expressed as

$$\frac{\partial u_i}{\partial t} = -u_j \frac{\partial u_i}{\partial x_j} - \frac{1}{\rho}\frac{\partial p}{\partial x_i} + \frac{2}{\rho}\frac{\partial}{\partial x_j}\left[\left(\mu(S_{ij} - \frac{1}{3}S_{kk}\delta_{ij}\right)\right] + \frac{1}{\rho}\frac{\partial}{\partial x_i}\left(\frac{5}{3}\mu S_{kk}\right). \tag{5.5.1}$$

The above equation can also be expressed as

$$\frac{\partial u_i}{\partial t} = \mathcal{T}_i + \mathcal{P}_i + \mathcal{V}_i + \mathcal{D}_i, \tag{5.5.2}$$

where, the nonlinear advective processes $\mathcal{T}_i$, pressure gradient effects $\mathcal{P}_i$, shear viscous diffusion $\mathcal{V}_i$, and dilatational viscous effects $\mathcal{D}_i$ are given by

$$\mathcal{T}_i = -u_j \frac{\partial u_i}{\partial x_j}, \tag{5.5.3}$$

$$\mathcal{P}_i = -\frac{1}{\rho}\frac{\partial p}{\partial x_i}, \tag{5.5.4}$$

$$\mathcal{V}_i = \frac{2}{\rho}\frac{\partial}{\partial x_j}\left[\mu\left(S_{ij} - \frac{1}{3}S_{kk}\delta_{ij}\right)\right], \tag{5.5.5}$$

$$\mathcal{D}_i = \frac{1}{\rho}\frac{\partial}{\partial x_i}\left(\frac{5}{3}\mu S_{kk}\right). \tag{5.5.6}$$

After employing the 2D Fourier transform along the homogeneous transverse (x_2 and x_3) directions [13], we get the velocity spectrum given by

$$\frac{\partial \widehat{u_i}}{\partial t} = \widehat{\mathcal{T}_i} + \widehat{\mathcal{P}_i} + \widehat{\mathcal{V}_i} + \widehat{\mathcal{D}_i}. \tag{5.5.7}$$

The velocity spectrum is a function of the 2D wave vector, k_p, streamwise coordinate, x_1, and time, t. Furthermore, the SKE at a location in the flame brush corresponding to the progress variable, c, can be defined as $\widehat{E}(k_p, x_1, t, c) = \frac{1}{2}\widehat{u}_i^*\widehat{u}_i$, where $\widehat{(\cdot)}^*$ represents the complex conjugate. Conditioning the spectra onto the spatially averaged progress variable gives the equation for the SKE

$$\frac{\partial \widehat{E}}{\partial t} = \widehat{\mathrm{T}} + \widehat{\mathrm{P}} + \widehat{\mathrm{V}} + \widehat{\mathrm{D}}. \tag{5.5.8}$$

The terms in the above equation are no longer dependent on x_1 due to the spatial averaging and the direct relationship between x_1 and c. These terms can be generally defined as $\widehat{G}(k_p, c, t) = \left[\frac{1}{2}(\widehat{u}_i^* \widehat{\mathcal{G}}_i + \widehat{u}_i \widehat{\mathcal{G}}_i^*)|c\right]$, where $\widehat{G}$ represents $\widehat{\mathrm{T}}$, $\widehat{\mathrm{P}}$, $\widehat{\mathrm{V}}$, or $\widehat{\mathrm{D}}$, and $\widehat{\mathcal{G}}_i$ represents $\widehat{\mathcal{T}}_i$, $\widehat{\mathcal{P}}_i$, $\widehat{\mathcal{V}}_i$, or $\widehat{\mathcal{D}_i}$ which are the Fourier transforms of Eqs. (5.5.3)-(5.5.6). Note that the turbulence length scales are represented by wavenumbers, k_p, which are inverse to the eddy length scale such that the smallest and largest wavenumbers represent the largest and smallest length scales, respectively.

Figure 5.14 shows the SKE distribution computed at $t/t_0 = 2$ along the instantaneous flame front defined by $c = 0.8$. Case A4 is shifted further toward high wavenumbers in the spectrum than the other cases. This shift can be attributed to Case A4 being at high pressure and initiated with a smaller integral length scale than the other cases. Note that this case also corresponds to the D/BRZ regime based on the initial conditions.

Examining the inertial subrange for the spectra in Fig. 5.14, one can easily see that the high-pressure cases show stretching of the spectrum. In these cases, the spectrum stretches towards higher wavenumbers (smaller scales), and it is most pronounced in Case A4. The stretching indicates that the smaller scales contribute more to the transfer of kinetic energy and are more energetic at elevated pressures than at atmospheric pressure, which agrees with the results of Fragner et al. [15].

The spectra for the transport terms at a location within the flame brush corresponding to $c = 0.8$ are shown in Fig.5.15. For Case A1, nonlinear advection ($\widehat{\mathrm{T}}$) contributes more than the other terms to interscale kinetic energy transfer at high wavenumbers (small scales).

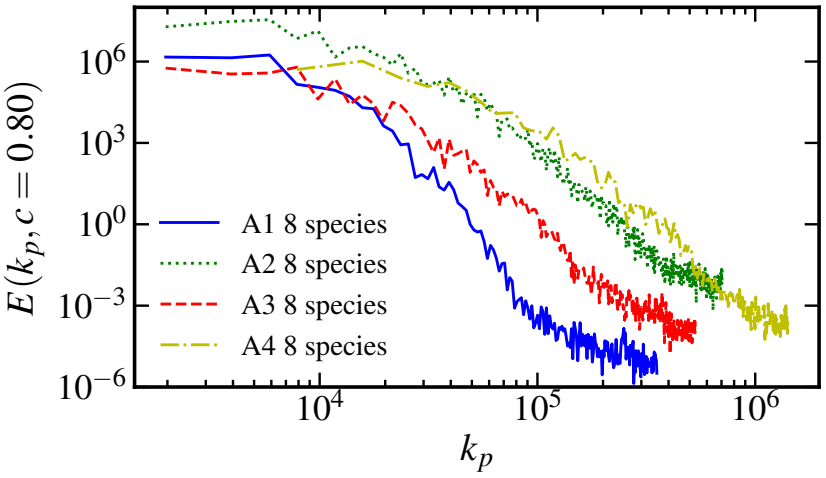

Figure 5.14 Spectral kinetic energy (SKE)

In contrast, at low wavenumbers (large scales), the viscous diffusion term ($\widehat{\mathrm{V}}$) contributes the most to kinetic energy transfer (Fig. 5.15 (a)). Pressure increase under a constant turbulent intensity and integral length scale, as seen in Figure 5.15 (b) results in an equal contribution from the viscous diffusion and advection terms, whereas the dilatational effects ($\widehat{\mathrm{D}}$) contribute the least to the interscale kinetic energy transfer. Additionally, the spectrum in Case A2 is stretched towards the small scales. Figure 5.15 (c) shows the spectra for Case A3, which is noticeably less stretched than in Case A2 due to a relatively lower initial Reynolds number of this case. In Case A3, the transport terms display similar behavior until the smallest scales, where the advection term contributes the most to kinetic energy transfer. Case A4 displays the most significant stretching of the spectrum. In particular, the advection and viscous diffusion terms are stretched more than the pressure gradient and dilatational terms and contribute more in the smallest length scales.

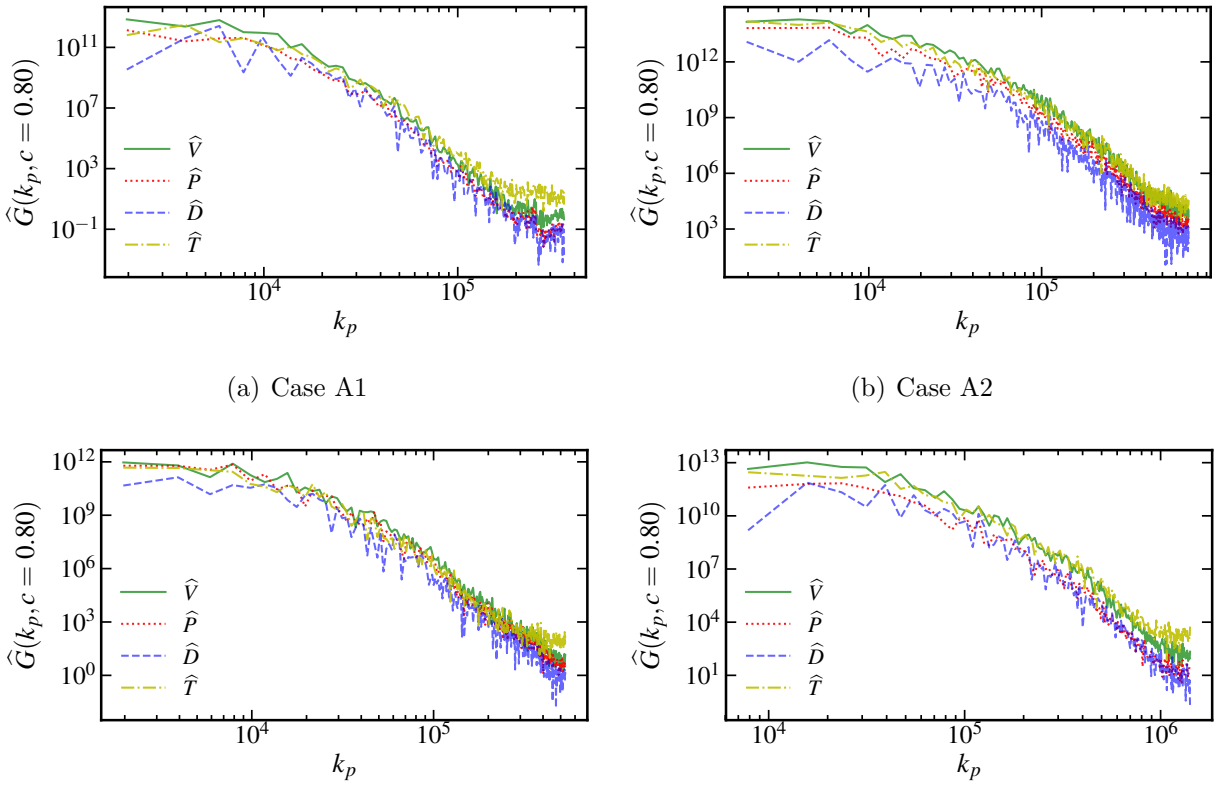

(a) Case A1

(b) Case A2

(c) Case A3

(d) Case A4

Figure 5.15 Spectra for the transport terms

Overall, these results indicate that the advection and the viscous diffusion terms play an essential role in the interscale kinetic energy transfer at elevated pressure. The increase in pressure also corresponds to a prevalence of small scales of motion, where again, both these terms contribute significantly more than the pressure gradient and the dilatation effects.

CHAPTER 6

EFFECTS OF COMPLEXITY OF FINITE-RATE CHEMISTRY

It has been previously suggested [24] that the behavior of turbulent flames at atmospheric conditions can be accurately predicted by knowing only a few laminar flame properties, regardless of the chemical model used. However, several of the past studies have shown the effects of chemical models on turbulence-chemistry interactions. Furthermore, it has recently been hypothesized that local chemical pathways may also be sensitive to the effects of pressure [53]. Therefore, this chapter compares the results from the moderately complex 8-species and 4-step mechanism [41] and the skeletal 13-species and 73-step mechanism [36] for cases A1 and A4. The 13-species mechanism is known to provide accurate results similar to what is obtained experimentally, therefore this mechanism is used as a reference for the comparisons in this chapter. The discussion of the results in this chapter will focus on how the complexity of the chemical mechanism affects turbulence-chemistry interactions at pressures of 1 and 10 atm while keeping the length-scale ratio, l_t/δ_{L}, fixed with the same background turbulence intensity, u'.

First, the flame structure are discussed in Sec. 6.1, and then the spatially averaged statistics are presented in Sec. 6.2. Next, the effects of finite-rate chemistry on the conditional statistics are discussed in Sec. 6.3. Afterward, the statistics of curvature and heat-release rate are described in Sec. 6.4. Finally, the spectral characteristics are presented in Sec. 6.5.

6.1 Structural Features of Flow and Flame

This section evaluates the effects of finite-rate chemistry on structural features of flow and flame. Similar to Sec. 5.1, the instantaneous flame and flow structures are examined at $t/t_0 = 2$ in terms of contours of the progress variable, temperature, and vorticity magnitude in the central $x_1 - x_2$ plane.

Figure 6.1 shows the contours of c with the axes being made dimensionless as described in Sec. 5.1. It is worth noting that the mean global flame position x_0 for Case A1 is the same for both chemical mechanisms, but it changes for Case A4 with values of $x_0 = 0.000318$ and $x_0 = 0.000279$ for the 8-species and 13-species mechanisms, respectively.

In Figure 6.1, the solid, black curve near the center of the domain indicates the location of the instantaneous flame front defined by the iso-value of the progress variable, i.e., $c = 0.8$. In Case A1, the flame-turbulence interaction leads to distortion of the initially planar flame structure, but the distortion is less intense in the 13-species case as seen in Fig. 6.1 (c). Furthermore, the reaction zone is thicker, and the progress variable gradient is reduced in the 13-species configuration.

Turbulence-flame interactions at high-pressure with same length-scale ratio (l_t/δ_L) results in a thicker flame brush as observed for Case A4 in Fig. 6.1 (b). The 13-species configuration of Case A4 also displays a broader flame brush, but there are much finer turbulent structures present, and the flame front is much more distorted than in the 8-species configuration. Further examination of Fig. 6.1 (d) shows pockets of unburnt and partially-burnt gas within the preheat and reaction zones, and there are partially burnt

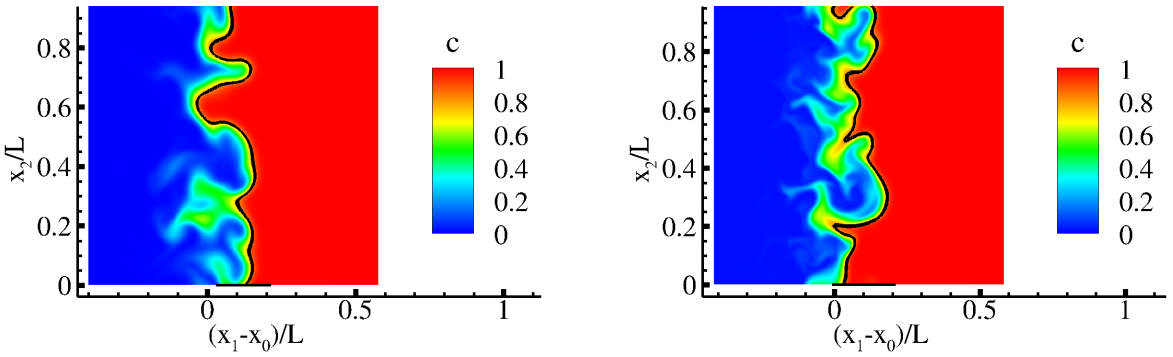

(a) Case A1 (8 species)

(b) Case A4 (8 species)

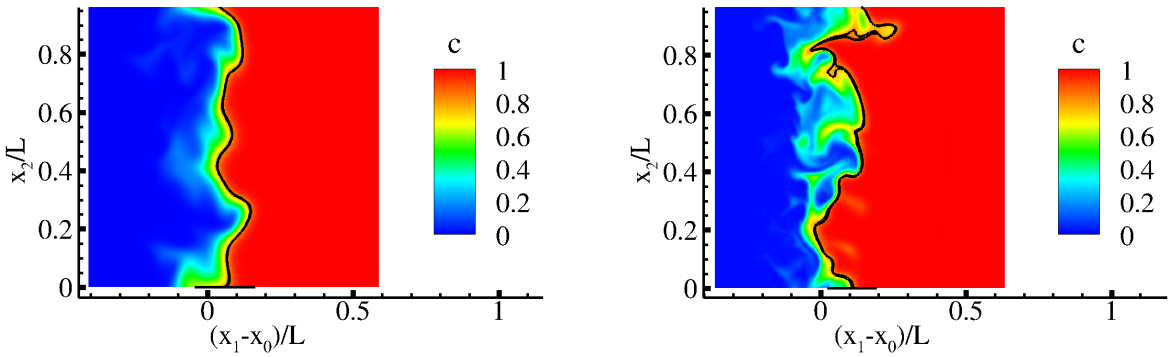

(c) Case A1 (13 species)

(d) Case A4 (13 species)

Figure 6.1 Instantaneous contours of the progress variable, c, in the central $x_1 - x_2$ plane at $t/t_0 = 2$

gases in the products. The reaction zone thickness varies drastically, and in some regions, the reaction zone is discontinuous. For Case A4, the progress variable gradient varies significantly throughout the flame front for the 13-species configuration. Qualitatively, the complexity of the chemical mechanism affects the flame structure in the preheat and reaction zones. In particular, these effects are more prevalent in high-pressure conditions.

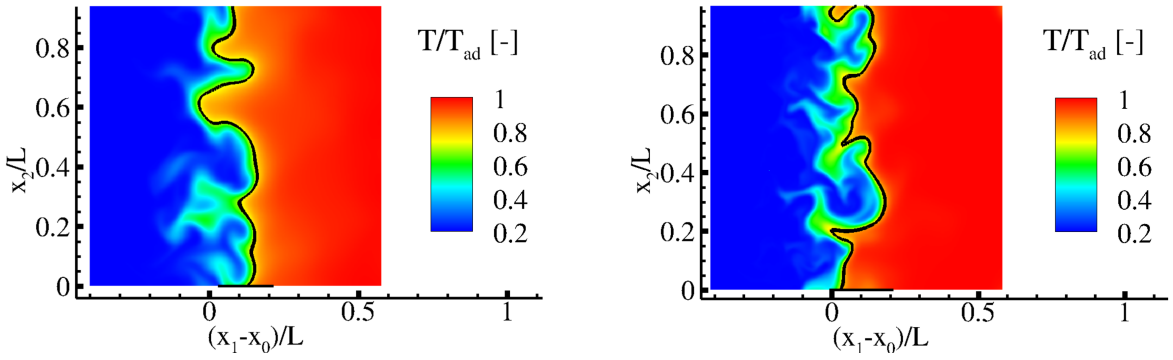

(a) Case A1 (8 species)

(b) Case A4 (8 species)

(c) Case A1 (13 species)

(d) Case A4 (13 species)

Figure 6.2 Instantaneous contours of the normalized temperature (T/T_{ad}) in the central $x_1 - x_2$ plane at $t/t_0 = 2$

Figure 6.2 shows the contours of normalized temperature, where the normalization is performed by the adiabatic flame temperature, T_{ad}. The case at atmospheric pressure, i.e., Case A1, is shown in Fig. 6.2 (a) and (c) and displays a smooth temperature gradient around

the reaction zone, with the 13-species configuration displaying nearly the same temperature gradient. However, qualitatively, the 13-species configuration exhibits a reduced degree of distortion in the flame structure than the 8-species configuration.

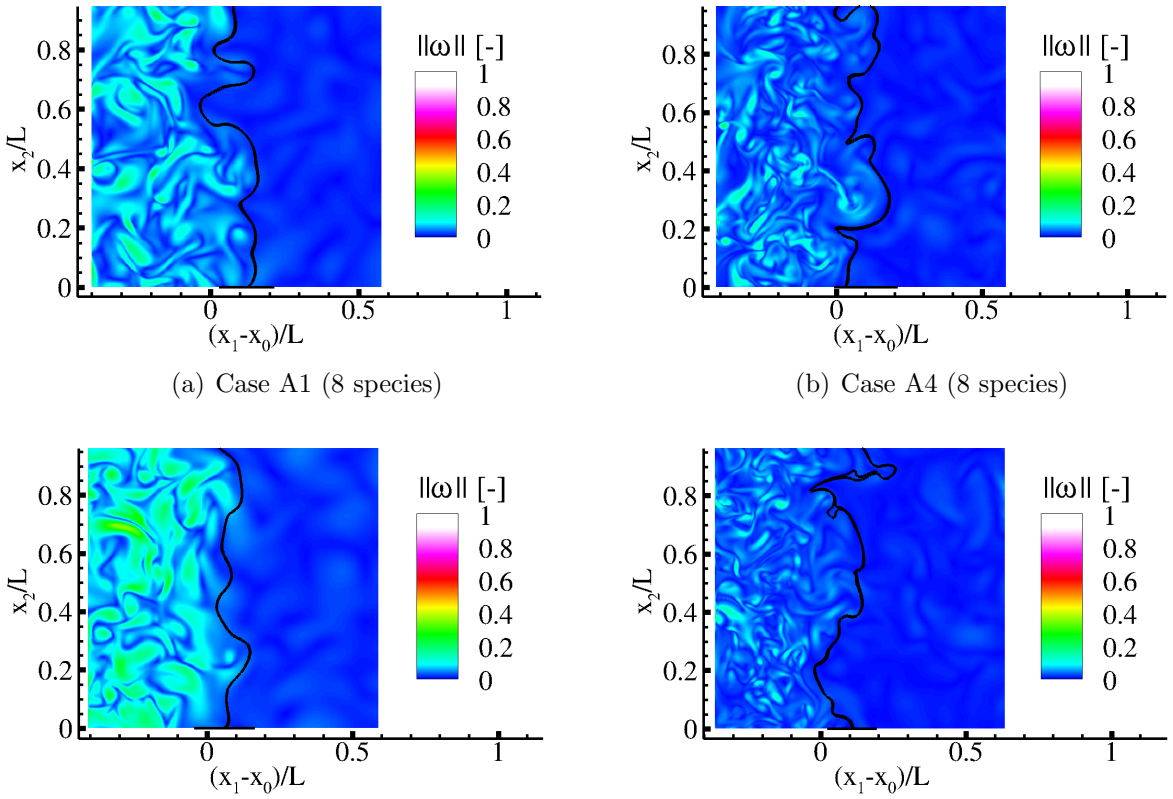

(a) Case A1 (8 species)

(b) Case A4 (8 species)

(c) Case A1 (13 species)

(d) Case A4 (13 species)

Figure 6.3 Instantaneous contours of vorticity magnitude in the central $x_1 - x_2$ plane at $t/t_0 = 2$

As discussed in Sec. 5.1, the flame brush thickening causes a broader temperature distribution in Case A4 due to the flame brush's homogenization due to enhanced heat and mass transport. However, in the 13-species configuration for Case A4, the temperature gradient varies significantly, and the fine-scale wrinkling of the flame structure is also enhanced. Overall, the flame brush tends to be sharper in the 13-species configuration due to a reduced

level of homogenization within the preheat zone. This is true for both pressure conditions.

The contours of the instantaneous vorticity magnitude are shown in Fig. 6.3 where the vorticity magnitude is non-dimensionalized by the corresponding peak vorticity magnitude for each case. Figure 6.3 (a) shows how Case A1 is characterized by small-scale turbulent structures in the preheat region that do not penetrate past the flame front, which is also observed in the 13-species configuration in Figure 6.3 (c). However, qualitatively, the vorticity gradient is more intense in the 13-species case. In Case A4, the flow structures are very similar to Case A1. Similarly, these structures do not penetrate the innermost layer of the flame, as shown in Fig. 6.3 (b) due to an increase in the viscosity near the flame region and the post-flame region. The vorticity magnitude contours for the 13-species configuration of Case A4 shown in Fig. 6.3 (d) again exhibit the presence of a more intense vorticity gradient. In Case A1 and Case A4, the 13-species configurations display sharper gradients of the vorticity magnitude in the flame and post-flame regions.

The instantaneous flame and flow structures discussed in this section highlight the role of complexity of the chemical model on the highly nonlinear flame-turbulence interactions of turbulent premixed flames. The effects of finite-rate chemistry are most pronounced for the high pressure case. The following sections examine these effects quantitatively.

6.2 Spatially Averaged Statistics

In this section, the spatially averaged statistics of Case A1 and Case A4 are examined. As explained before in Section 5.2, the spatially averaged statistics are obtained by averaging along the homogeneous x_2 (y)- and x_3 (z)-directions, which is defined in Eq. (5.2.1). The

x-axis has been made dimensionless following the same approach as in Section 5.2. The results in this section are compared after the evolution of the flame-turbulence interactions for two eddy turnover times.

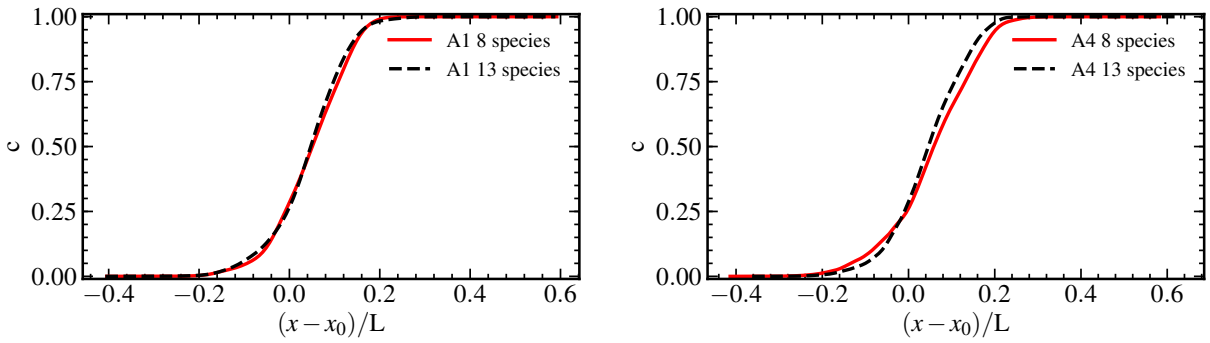

(a) Case A1

(b) Case A4

Figure 6.4 Spatially averaged profile of the progress variable, c

Examining the spatial variation of the average progress variable in Fig. 6.4 (a) shows that both chemical mechanisms are in good agreement with each other for Case A1, showing only minor sensitivity to the chemical model. In contrast, for Case A4, the slope of the distribution is steeper in the 13 species configuration. This indicates that a simpler chemistry model predicts a thicker flame brush at elevated pressure, which may be caused by overprediction of the effects of homogenization within the flame brush. These results are consistent with the instantaneous flame structure shown in Figs. 6.1 and 6.2. The role of the chemical mechanism on the flame structure is significant as pressure is increased.

The spatially averaged temperature field in Fig. 6.5 also exhibits similar effects to the chemical model, where the effects are more pronounced in the higher pressure case. This is due to a correlation of the progress variable and the temperature fields as discussed in Ch. 5.

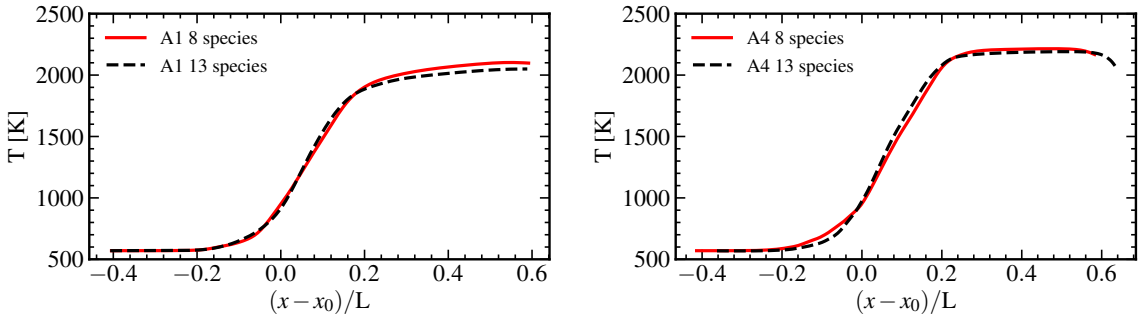

(a) Case A1 (b) Case A4

Figure 6.5 Distribution of spatially averaged temperature field

To examine the effects of the chemical model on the intermediate species, the spatial variation of the averaged mass fraction of CO is shown in Fig. 6.6. Sec. 5.2 discussed that Case A1 contains CO in its products because of the slower increase in the temperature within the post-flame region. Similar results are observed in the 13-species configuration of Case A1 as well. The 8-species configuration overpredicts the mass fraction of CO in the flame region and underpredicts the mass fraction of CO in the products.

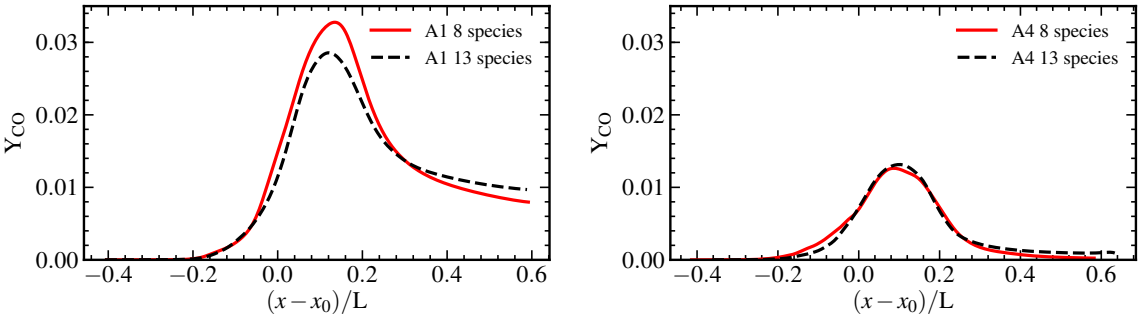

(a) Case A1 (b) Case A4

Figure 6.6 Spatially averaged profile of mass fraction of the intermediate species, CO

In Case A4, the simpler chemistry model predicts complete oxidation of carbon monoxide to CO_2 in the post-flame zone. This likely occurs because Case A4 reaches and maintains the maximum flame temperature early in the post-flame zone, and as a result, CO is completely oxidized. However, the 13-species case shows a slightly different outcome. By examining Fig. 6.6 (b), we can see that the 13-species case predicts the mass fraction of CO in the products to be about 0.0015, indicating the effects of the chemical mechanism on the intermediate species.

This section shows that the spatially averaged statistics of both major and minor species are sensitive to the employed chemical model. The sensitivity is enhanced, particularly with an increase in pressure.

6.3 Statistical Features of Flame-Turbulence Interaction

The effects of the chemical model on the flame-turbulence interactions in the state-space are now examined. We examine the variation of the fuel reaction rate, $\dot{\omega}_{CH_4}$ and the mass fraction of CO with respect to the progress variable, c, in this section.

The conditionally averaged $\dot{\omega}_{CH_4}$ with respect to c is shown in Fig. 6.7. The effects of the chemical model on the variation of the reaction rate are evident in both cases. In particular, in Case A1 at atmospheric conditions, the reaction rate distribution is steeper, and the magnitude of the peak reaction rate is higher in the 8-species configuration. This is consistent with a higher laminar flame speed predicted by the 8-species mechanism compared to the 13-species mechanism under the chosen operating conditions. At elevated pressure, there is significant variation in the behavior of the reaction rate. For example, Case A4

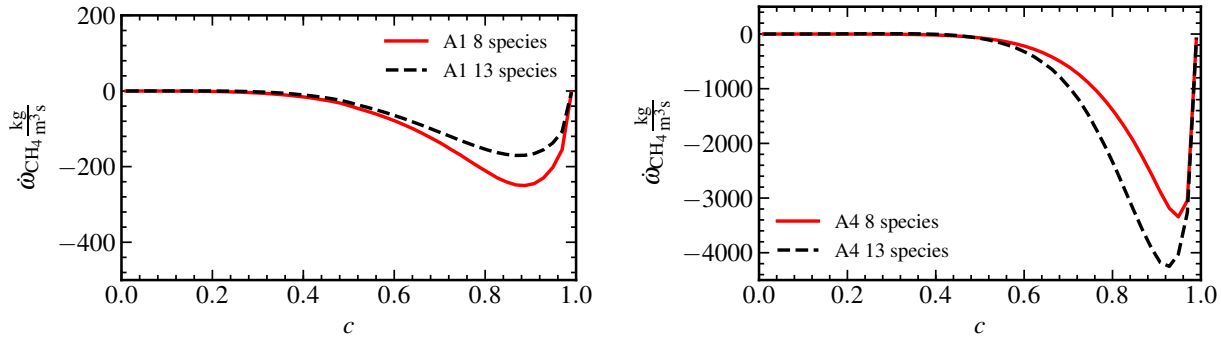

(a) Case A1 (b) Case A4

Figure 6.7 Reaction rate of methane conditionally averaged with respect to the progress variable

displays a steeper distribution and a higher peak reaction rate in the 13-species configuration. Furthermore, while the peak reaction rate magnitude occurs at about $c = 0.96$ for the 8-species case and at about $c = 0.92$ for the 13-species case. The variation of the reaction rate for Case A4 is likely attributed to more intermediate species in this mechanism.

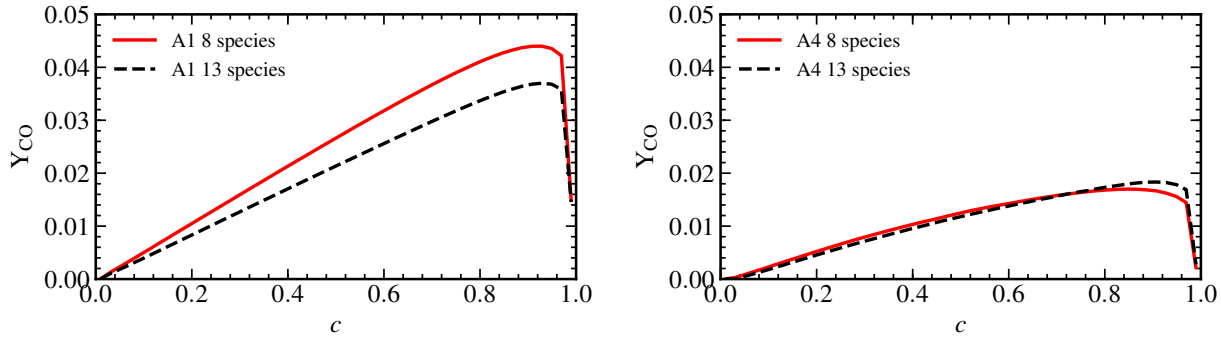

(a) Case A1 (b) Case A4

Figure 6.8 Mass fraction of the intermediate species, CO, conditionally averaged with respect to the progress variable

The conditionally averaged mass fraction of CO with respect to c are shown in Fig. 6.8. The distribution in Case A1 is nearly linear for both chemical mechanisms for $c \lessapprox 0.8$. However, the variation of Y_{CO} is steeper in the 8-species configuration, indicating that the simpler chemical model overpredicts the mass fraction of CO. For Case A4, the two chemical mechanisms present almost identical results until around $c = 0.76$, where the 8-species case underpredicts the mass fraction of CO.

These results again indicate the effects of the employed chemical model on the variation of the major and the minor species in the state space, thus necessitating the requirement to use a detailed chemical mechanism to accurately predict the species distribution, particularly within the flame brush region.

6.4 Curvature and Heat Release Rate Statistics

Now, we examine the effects of the complexity of the chemical mechanisms on the variation of the flame curvature, κ, and the conditionally averaged heat release rate (HRR). We also investigate how the chemistry affects the dependence of HRR on flame curvature.

Figure 6.9 shows the PDF of flame curvature for cases A1 and A4, and the measures of central tendency are summarized in Table 6.1. The flame curvature's PDF is computed at the instantaneous flame front, which is identified using the progress variable at $c = 0.8 \pm 0.125$

The PDFs for the two configurations of Case A1 shown in Fig. 6.9 (a) are both positively skewed, but the simpler chemical model is more skewed. At atmospheric pressure, using a more complex chemical model results in a 29% decrease in skewness and a 19% decrease in standard deviation. The 8-species case has a mean of $\mu = 0.47$ and the 13-species

case has a mean of $\mu = 0.31$. This variation indicates that the 8-species mechanism produces a broader, more skewed PDF at atmospheric pressure and overpredicts the probability of a large magnitude of curvature.

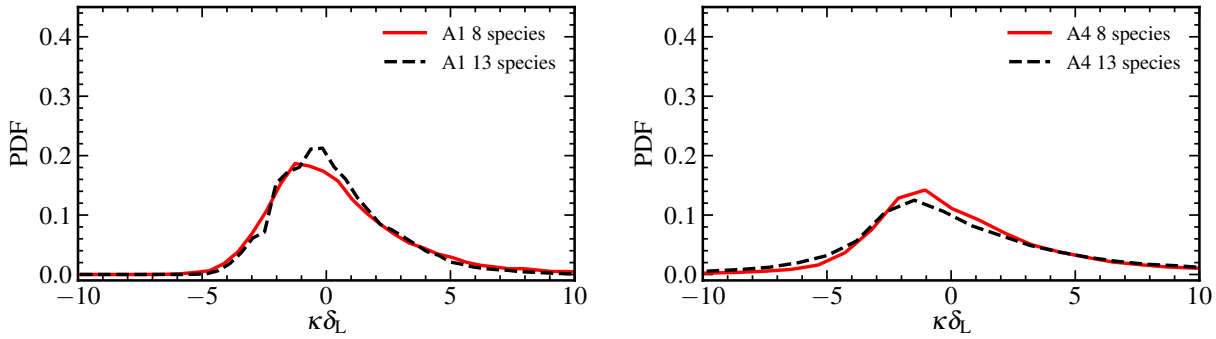

(a) Case A1 (b) Case A4

Figure 6.9 Probability density function (PDF) of the flame curvature at the instantaneous flame front

Table 6.1 Measures of central tendency for the flame curvature

Case	μ	σ	γ
A1 8-species	0.47	2.82	1.33
A1 13-species	0.31	2.29	0.95
A4 8-species	1.11	5.29	1.78
A4 13-species	0.85	5.72	1.28

Figure 6.9 (b) shows the PDFs for the two configurations of Case A4, which are both positively skewed. The measures of central tendency are summarized in Table 6.1. For

case A4, using a more complex chemical mechanism results in a 28% decrease in skewness. Similar to Case A1, the mean of the 8-species case is shifted further to the right with $\mu = 1.11$ compared to the 13-species case where $\mu = 0.85$. Despite these similarities between Case A1 and Case A4, the complexity of the chemical model has a different effect on the standard deviation in Case A4. In this case, using a more complex chemical model results in an 8.3 % increase in standard deviation.This indicates that the 8-species mechanism produces a more skewed, narrower PDF and underpredicts the probability of a large curvature magnitude at elevated pressure.

In Figure 6.10, the non-dimensional HRR conditionally averaged on the progress variable is shown for cases A1 and A4. This figure shows that the chemical mechanism's complexity affects the HRR, and these effects are different with respect to pressure. In Case A1, the distribution of HRR is the most affected in the lower temperature regions where the 8-species case predicts a much higher value than the 13-species case. However, the distributions of the HRR using the two chemical mechanisms nearly collapse in the higher temperature regions.

On the other hand, at higher pressure, as evident from Fig. 6.10 (b), the distribution of HRR is unaffected by the complexity of the chemical mechanism in the lower temperature regions. Still, there are variations in the distributions near the flame front in the higher temperature regions. The 8-species case underpredicts the HRR in these high-temperature regions and slightly overpredicts the shift in the peak burning towards higher temperature. Furthermore, at elevated pressure, there are differences in the peak values. In particular, the

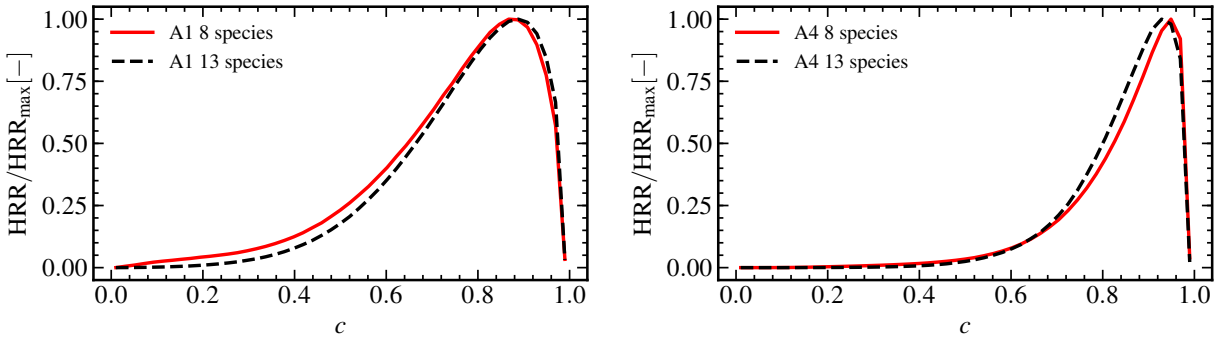

(a) Case A1

(b) Case A4

Figure 6.10 Conditional variation of HRR with respect to the progress variable

13-species case results in a broader peak than the 8-species case. This indicates the highest HRR values may actually occur over a wider range of temperatures.

The variation of HRR with respect to the flame curvature is now examined by plotting the scatter of the HRR against the normalized flame curvature at the flame front, which is shown in Fig. 6.11. All four cases have a moderate yet negative correlation between HRR and curvature. However, the behavior of this correlation varies in each case. For example, Fig. 6.11 (a) shows the scatter for the 8-species configuration of Case A1. In this figure, it is clear that Case A1 displays a stronger negative correlation in the negative curvature regions and more scatter in the positive regions. A similar trend is difficult to characterize for the 13-species case in Fig. 6.11 (c). The 13-species display a distinct negative relationship between HRR and curvature, but there is minimal variation in the density and spread of the scatter. For both cases at atmospheric pressure, the maximum HRR values occur in the regions of the highest negative curvature.

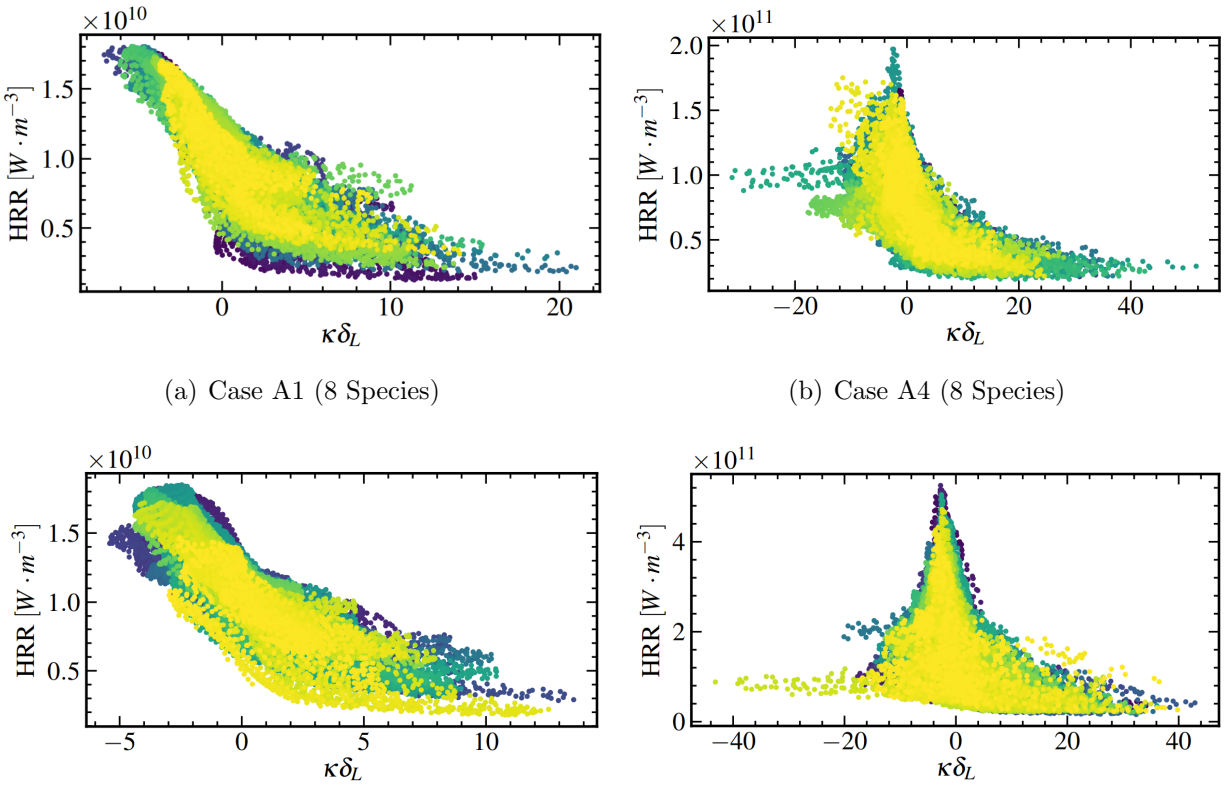

(a) Case A1 (8 Species)

(b) Case A4 (8 Species)

(c) Case A1 (13 Species)

(d) Case A4 (13 Species)

Figure 6.11 Scatter of HRR with respect to the flame curvature

At elevated pressure, Case A4 displays a stronger correlation in the positive curvature regions and an increase in the scatter in the negative curvature regions as shown in Fig. 6.11 (b). This trend is even more pronounced in the 13-species configuration of Case A4. At elevated pressure, both chemical mechanisms result in the maximum HRR values occurring around $\kappa\delta_L = 0$. This is the most apparent in the 13-species case where Fig. 6.11 (d) shows a sharp peak in HRR at $\kappa\delta_L = 0$.

The differences in the relationships between HRR and curvature are even more apparent when the heat release rate is conditionally averaged on the flame curvature. Figure 6.12

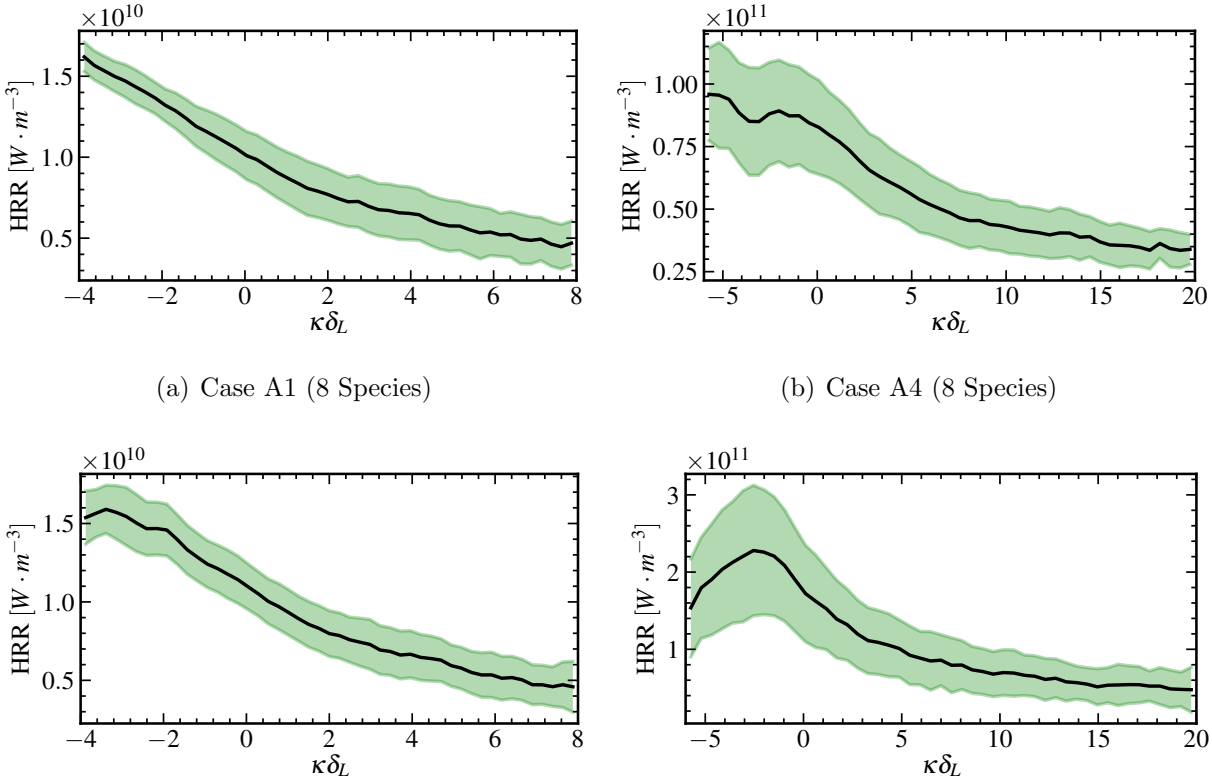

(a) Case A1 (8 Species)

(b) Case A4 (8 Species)

(c) Case A1 (13 Species)

(d) Case A4 (13 Species)

Figure 6.12 HRR conditioned on curvature with descriptive statistics

shows the conditionally averaged HRR with respect to κ where the green regions are $\pm$ one standard deviation away from the averaged HRR. In Case A1, both the chemical models show a monotonic decrease in the mean HRR with respect to κ. However, the behavior of the standard deviation is different. For example, In Fig. 6.12 (a), it is evident that the standard deviation is the largest in the positive curvature regions and smallest in the negative curvature regions for the 8-species configuration of Case A1. However, the 13-species configuration does not show any significant changes in standard deviation from the negative to the positive curvature regions.

The mean HRR monotonically decreases in the regions of positive curvature in Case A4 for both chemical mechanisms. However, a non-monotonic variation of the mean HRR occurs in the negative curvature region. Furthermore, there are clear differences in the variation of HRR, particularly in the negative curvature region, while using different chemical models. In addition, both configurations for Case A4 display the opposite behavior at elevated pressure, with standard deviation being the largest and smallest in the negative and positive curvature regions, respectively. Finally, there is a significant increase in the standard deviation around the peak of HRR for the 13-species case.

This section demonstrated the role of the chemical model on the flame characteristics in terms of curvature, HRR, and their relationship. Furthermore, the effects of chemistry show significant variation as the pressure is increased, which can be attributed to highly nonlinear turbulence-chemistry interactions prevalent in such a canonical chemically reacting flow.

6.5 Comparison of Spectral Characteristics

This section examines the effects of the complexity of chemical mechanisms on the spectral characteristics of kinetic energy. The spectra for kinetic energy are obtained following the methods outlined in Sec. 5.5.

Figure 6.13 shows the spectral kinetic energy computed at the second eddy turnover time along the instantaneous flame front defined by $c = 0.80$ for cases A1 and A4. Recall from Sec. 5.5, that the length scales are represented by wavenumbers which are inverse to the eddy length scale such that the smallest and largest wavenumbers represent the largest

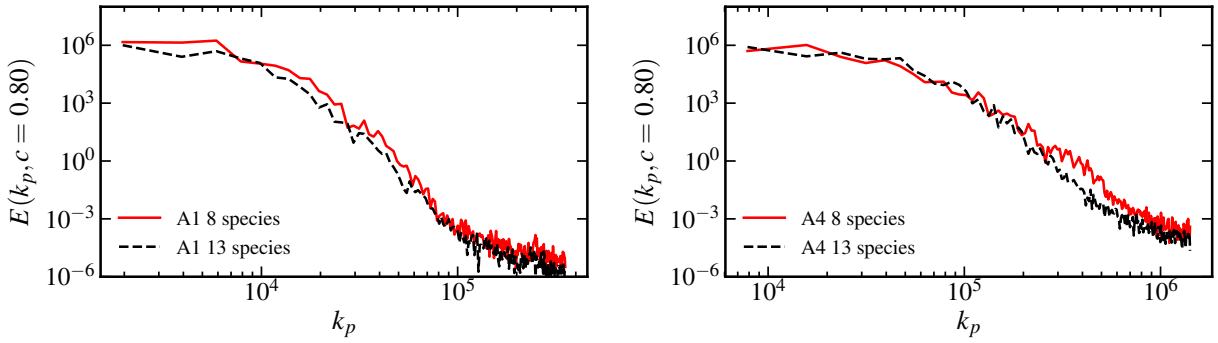

(a) Case A1

(b) Case A4

Figure 6.13 Spectral.kinetic energy (SKE)

and smallest length scales, respectively. For Case A1 in Fig. 6.13 (a), the spectrum displays noticeable variations between the two chemical mechanisms. In particular, the 13-species chemical mechanism predicts a lower energy content that is most noticeable in the intermediate scales. At elevated pressures, the spectrum stretches towards higher wavenumbers (smaller scales) as seen in Fig. 6.13 (b) for Case A4. The spectrum for the 13-species case is also stretched towards the smaller scales but predicts a much lower energy content. The difference in energy content is most pronounced for the small length scales, where the difference in energy content can be up to an order of magnitude.

The variations in the spectral characteristics of cases A1 and A4 suggest that the energy spectrum is sensitive to both elevated pressure and the complexity of the chemical mechanism employed. The simpler chemical mechanism overpredicts the energy contained within the intermediate length scales at atmospheric pressure. At high pressure, it overestimates the energy content of the small length scales by up to an order of magnitude.

CHAPTER 7

CONCLUSIONS

In this chapter, the key findings of this study are highlighted in terms of the key technical objectives described in Sec. 1.1, and then the future scope of the present work is outlined.

7.1 Key Findings

The key findings of this study are as follows:

- **Characterize the effects of pressure on:**
  - **Structural features:** An increase in pressure leads to a severe disruption of the flame structure by the turbulent eddies and decreased flame thickness and flame speed. However, increasing pressure while maintaining a constant length scale ratio leads to reduced wrinkling and instability, likely caused by turbulence-flame interactions resulting in smaller-scale eddies causing enhanced heat and mass transport and homogenization within the flame brush region.
  - **Statistical features:** The spatial distributions of temperature and the progress variable are affected by increased pressure. The pressure increase causes narrower distributions except in the case of maintaining a constant length scale ratio, again indicating the enhanced homogenization effect of the turbulent eddies. For all high-pressure cases, the mass fractions of the intermediate species were reduced

when pressure increased. It was also observed that increasing pressure significantly increases the maximum reaction rate magnitude and results in a sharper reaction rate variation. Furthermore, increasing pressure causes a higher positive correlation between temperature and the progress variable.

  - **HRR and curvature:** At elevated pressure, the PDF of curvature became broader except in the case of maintaining a constant velocity scale ratio where the PDF became narrower. When comparing the high-pressure cases only, it is clear that the probability for large curvature and skewness increases with increasing Karlovitz number. Increasing pressure shifts the peak burning towards higher temperature regions and affects the relationship between HRR and flame curvature. The standard deviation of HRR is the largest in the negative curvature regions for the high-pressure cases.
  - **Spectral characteristics:** Comparing the two-dimensional spectral kinetic energy of the cases showed that increasing pressure causes the spectrum to shift towards the higher wavenumbers, indicating that the smaller scales are more energetic at elevated pressures. Overall, the advection and viscous diffusion terms contribute more to the transport of the spectral kinetic energy than the pressure gradient and dilatational terms and the contributions are more in the smallest length scale.

- **Characterize the effects of finite-rate chemistry on:**
  - **Structural features:** The effects of the complexity of chemical mechanism on the flame structure in the preheat and reaction zone are more prevalent in the high-

pressure condition. It is observed that the 13-species mechanism results in a much more distorted flame front with significant variation in reaction zone thickness and progress variable gradient. In contrast to the case at atmospheric pressure, the 13-species configuration exhibits a reduced level of distortion. At elevated pressure, the flame brush tends to be sharper in the 13-species configuration due to a reduced level of homogenization within the preheat zone.

- **Statistical features:** At elevated pressure, the spatial distributions of temperature and progress variable are affected by increased pressure, indicating that a simpler chemistry model predicts a thicker flame brush at high pressure, which may be caused by overprediction of the effects of homogenization within the flame brush. Furthermore, a more detailed chemical mechanism is needed to accurately predict the major and minor species distributions. The effects of the chemical model on the variation of the reaction rate are evident in both cases, but it is more pronounced at high pressure.
- **HRR and curvature:** Flame curvature are sensitive to the complexity of the chemical model at both pressures. In particular, the simpler chemical mechanism overpredicts the probability for large curvature at atmospheric pressure and underpredicts it at elevated pressure. At elevated pressure, the 8-species case underpredicts the HRR in these high-temperature regions and slightly overpredicts the shift in the peak burning towards higher temperature. It is also observed that the relationship between HRR and flame curvature is sensitive to the complexity of the chemical model at elevated pressure.

– **Spectral characteristics:** Examining the two-dimensional spectral kinetic energy for the two chemical mechanisms suggests that the energy spectrum is sensitive to the complexity of the chemical model employed. For example, there is more variation in the spectra at elevated pressure, where the simpler chemical model overestimates the energy content of the small length scales by up to an order of magnitude.

7.2 Future Outlook

The aim of this thesis is to contribute to the fundamental understanding of the effects pressure and chemistry on the features of turbulent premixed flames. This research can be extended in many different ways. Some of the directions that one can pursue in the future are summarized below:

- **Extend the analysis to even higher pressures and realistic fuels:** The demand for clean combustion technologies, such as ultra high efficiency gas turbines, is expected to rise over the next couple of decades. Higher efficiency gas turbines will require even higher gas pressures. For example, even the latest industrial gas turbines require gas at pressures around 40 atm. Therefore, extending this analysis to further industry-relevant pressure and heavier hydrocarbon-based fuels could be the subject of future work.

- **Examine the effects of pressure and chemistry while employing more detailed chemical mechanisms:** In the current study, it has been shown that the complexity of the chemical mechanism does affect the DNS predictions. Furthermore,

there are differences in these effects at atmospheric pressure and elevated pressure. These effects are more pronounced at high pressure. Therefore, employing a more complex chemical mechanism would further clarify the effects of pressure on turbulent premixed flames.

- **Compare flame-turbulence interactions for decaying and forced turbulence conditions:** In the current study, a decaying background turbulence has been considered. There have been several recent studies where the background turbulence is artificially forced to maintain the level of turbulence to a quasi-stationary state. Therefore, the effects of pressure and finite-rate chemistry on the flame turbulence interactions can be examined for the decaying and statistically stationary scenario.
- **Analyze the DNS datasets for subgrid model development:** The high-fidelity DNS datasets generated in this study can be used for the assessment and development of advanced subgrid models for large-eddy simulations. Note that LES is a viable computational strategy for the study of practically relevant combustion devices. While there are several subgrid models available for LES, there are associated challenges. The DNS datasets can be used to assess the efficacy of some of the well-established closures.

REFERENCES

[1] Alqallaf, A., Klein, M., Dopazo, C., and Chakraborty, N. (2019). Evolution of flame curvature in turbulent premixed bunsen flames at different pressure levels. *Flow Turbulence Combust.*, 103:439–463.

[2] Aspden, A. J., Day, M. S., and Bell, J. B. (2011). Turbulence-flame interactions in lean premixed hydrogen: transition to the distributed burning regime. *J. Fluid Mech.*, 680:287–320.

[3] Carlsson, H., Yu, R., and Bai, X. (2014). Direct numerical simulation of lean premixed ch4/air and h2/air flames at high karlovitz numbers. *I. J. of Hydrogen Energy*, 39:20216–20232.

[4] Carlsson, H., Yu, R., and Bai, X. (2015). Flame structure analysis for categorization of lean premixed ch4/air and h2/air flames at high karlovitz numbers: Direct numerical simulation studies. *Proc. Combust. Inst.*, 35:1425–1432.

[5] Chen, J. H. (2011). Petascale direct numerical simulation of turbulent combustion—fundamental insights towards predictive models. *Proceedings of the Combustion Institute*, 33(1):99–123.

[6] Colin, O., Ducros, F., Veynante, D., and Poinsot, T. (2000). A thickened flame model for large eddy simulations of turbulent premixed combustion. *Physics of Fluids A*, 12:1843–1863.

[7] De Goey, L., Plessing, T., Hermanns, R., and Peters, N. (2005). Analysis of the flame thickness of turbulent flamelets in the thin reaction zones regime. *Proc. Combust. Inst.*, 30:859–866.

[8] Dinesh, K. R., Shalaby, H., Luo, K., van Oijen, J., and Thevenin, D. (2016). Effects of pressure on cellular flame structure of high hydrogen content lean premixed syngas sperical flames: A dns study. *Hy. Energy*, 41:21516–21531.

[9] Driscoll, J. F. (2008). Turbulent premixed combustion: Flamelet structure and its effect on turbulent burning velocities. *Prog. Energy Combust. Sci.*, 34(1):91–134.

[10] Driscoll, J. F., Chen, J. H., Skiba, A. W., Carter, C. D., Hawkes, E. R., and Wang, H. (2020). Premixed flames subjected to extreme turbulence: Some questions and recent answers. *Progress in Energy and Combustion Science*, 76:100802.

[11] Dunn, M., Masri, A., Bilger, R., Barlow, R., and Wang, G.-H. (2009). The compositional structure of highly turbulent piloted premixed flames issuing into a hot coflow. *Proc. Combust. Inst.*, 32:1779–1786.

[12] Dunn, M. J., Masri, M. J., and Bilger, R. W. (2007). A new piloted premixed jet burner to study strong finite rate chemistry effects. *Combust. Flame*, 151:46–60.

[13] Durran, D., Weyn, J. A., and Menchaca, M. Q. (2017). Practical considerations for computing dimensional spectra from gridded data. *Monthly Weather Review*, 145 issue 9:3901–3910.

[14] Echekki, T. and Chen, J. H. (1996). Unsteady strain rate and curvature effects in turbulent premixed methane-air flames. *Combust. Flame*, 106(2):184–202.

[15] Fragner, R., Halter, F., Mazellier, N., Chauveau, C., and Gokalp, I. (2015). Investigation of pressure effects on the small scale wrinkling of turbulent premixed bunsen flames. *Proc. Combust. Inst.*, 35:1527–1535.

[16] Gonzalez-Juez, E. D., Kerstein, A. R., Ranjan, R., and Menon, S. (2017). Advances and challenges in modeling high-speed turbulent combustion in propulsion systems. *Progress in Energy and Combustion Science*, 60:26–67.

[17] Goodwin, D. G., Moffat, H. K., and Speth, R. L. (2014). Cantera: An object-oriented software toolkit for chemical kinetics, thermodynamics, and transport processes. `http://www.cantera.org`. Version 2.1.2.

[18] Kim, W.-W. and Menon, S. (2000). Numerical modeling of turbulent premixed flames in the thin-reaction-zones regime. *Combustion Science and Technology*, 160(1):119–150.

[19] Klein, M., Nachtigal, H., Hansinger, M., Pfitzner, M., and Chakraborty, N. (2018). Flame curvature distribution in high pressure turbulent bunsen premixed flames. *Flow Turbulence Combust.*, 101:1173–1187.

[20] Kobayashi, H., Seyama, K., Hagiwara, H., and Ogami, Y. (2005). Burning velocity correlation of methane/air turbulent premixed flames at high pressure and high temperature. *Proc. Combust. Inst.*, 30:827–834.

[21] Kraichnan, R. H. (1970). Diffusion by a random velocity field. *Physics of Fluids*, 13:22–31.

[22] Lachaux, T., Halter, F., Chauveau, C., Gokalp, I., and Shepherd, I. (2005). *Proc. Combust. Inst.*, 30:819–826.

[23] Lapointe, S. and Blanquart, G. (2016). Fuel and chemistry effects in high karlovits premixed turbulent flames. *Combust. Flame*, 167:294–307.

[24] Lapointe, S., Savard, B., and Blanquart, G. (2015). Differential diffusion effects, distributed burning, and local extinctions in high karlovitz premixed flames. *Combustion and flame*, 162(9):3341–3355.

[25] Lu, Z. and Yang, Y. (2020). Modeling pressure effects on the turbulent burning velocity for lean hydrogen/air premixed combustion. *Proc. Combust. Inst.*, 000:1–8.

[26] MacCormack, R. W. (2003). The effect of viscosity in hypervelocity impact cratering. *Journal of spacecraft and rockets*, 40(5):757–763.

[27] Mansour, M. S., Peters, N., and Chen, Y. C. (1998). Investigation of local flame structures and statistics in partially premixed turbulent jet flames using simultaneous CH LIF/Rayleigh laser technique. *Proc. Combust. Inst.*, 27:767–773.

[28] Matalon, M. and Matkowsky, B. J. (1982). Flames as gas dynamic discontinuities. *J. Fluid Mech.*, 124:239–259.

[29] Panchal, A., Ranjan, R., and Menon, S. (2019). A comparison of finite-rate kinetics and flamelet-generated manifold using a multiscale modeling framework for turbulent premixed combustion. *Combustion Science and Technology*, 191(5-6):921–955.

[30] Peters, N. (2000). *Turbulent Combustion*. Cambridge University Press.

[31] Pitsch, H. (2006). Large-eddy simulation of turbulent combustion. *Annu. Rev. Fluid Mech.*, 38:453–482.

[32] Poinsot, T. and Veynante, D. (2005). *Theoretical and Numerical Combustion*. Edwards, Inc., second edition.

[33] Poludnenko, A. Y. and Oran, E. S. (2011). The interaction of high-speed turbulence with flames: global properties and internal flame structure. *Combust. Flame*, 157:995–1011.

[34] Ranjan, R., Muralidharan, B., Nagaoka, Y., and Menon, S. (2016). Subgrid-scale modeling of reaction-diffusion and scalar transport in turbulent premixed flames. *Combust. Sci. Technol.*, 188:1496–1537.

[35] Sankaran, R., Hawkes, E. R., Chen, J. H., Lu, T., and Law, C. K. (2007a). Structure of a spatially developing turbulent lean methane–air bunsen flame. *Proc. Combust. Inst.*, 31:1291–1298.

[36] Sankaran, R., Hawkes, E. R., Chen, J. H., Lu, T., and Law, C. K. (2007b). Structure of a spatially developing turbulent lean methane–air bunsen flame. *Proceedings of the combustion institute*, 31(1):1291–1298.

[37] Sankaran, V. and Menon, S. (2005). Subgrid combustion modeling of 3-D premixed flames in the thin-reaction-zone regime. *Proc. Combust. Inst.*, 30:575–582.

[38] Savard, B., Bobbitt, B., and Blanquart, G. (2015). Structure of a high karlovitz n-c 7 h 16 premixed turbulent flame. *Proceedings of the Combustion Institute*, 35(2):1377–1384.

[39] Savre, J., Carlsson, H., and Bai, X. S. (2013). Turbulent methane/air premixed flame structure at high karlovitz numbers. *Flow Turbulence Combust.*, 90:325–341.

[40] Sjöholm, J., Rosell, J., Li, B., Richter, M., Li, Z., Bai, X.-S., and Aldén, M. (2013). Simultaneous visualization of oh, ch, ch¡ sub¿ 2¡/sub¿ o and toluene plif in a methane jet flame with varying degrees of turbulence. *Proc. Combust. Inst.*, 34:1475–1482.

[41] Smith, T. M. and Menon, S. (1997). One-dimensional simulations of freely propagating turbulent premixed flames. *Combust. Sci. Technol.*, 128:99–130.

[42] Srinivasan, S. and Menon, S. (2014). Linear eddy mixing model studies of high karlovitz number turbulent premixed flames. *Flow Turb. Combust.*, 93:189–219.

[43] Steinberg, A. M., Hamlington, P. E., and Zhao, X. (2021). Structure and dynamics of highly turbulent premixed combustion. *Progress in Energy and Combustion Science*, 85:100900.

[44] Strakey, P., Sidwell, T., and Ontko, J. (2007). Investigation of the effects of hydrogen addition on lean extinction in a swirl stabilized combustor. *Proc. Combust. Inst.*, 31:3173–3180.

[45] Towery, C. A. Z., Poludnenko, A. Y., Urzay, J., O'Brien, J., Ihme, M., and Hamilngton, P. (2016). Spectral kinetic energy transfer in turbulent premixed reacting flows. *Phys. Rev. E*, 93:053115.

[46] Trouve, A. and Poinsot, T. (1994). The evolution equation for the flame surface density in turbulent premixed combustion. *J. Fluid Mech.*, 278:1–31.

[47] Wabel, T. M., Skiba, A. W., and Driscoll, J. F. (2017a). Turbulent burning velocity measurements: Extended to extreme levels of turbulence. *Proc. Combust. Inst.*, 36:1801–1808.

[48] Wabel, T. M., Skiba, A. W., Temme, J. E., and Driscoll, J. F. (2017b). Measurements to determine the regimes of premixed flames in extreme turbulence. *Proc. Combust. Inst.*, 36:1809–1816.

[49] Wang, H., Hawkes, E. R., Chen, J. H., Zhou, B., Li, Z., and Aldén, M. (2017). Direct numerical simulations of a high karlovitz number laboratory premixed jet flame–an analysis of flame stretch and flame thickening. *Journal of Fluid Mechanics*, 815:511–536.

[50] Wang, J., Guo, S., Zhang, W., Zhang, M., and Huang, Z. (2019). Effect of hydrogen ratio on turbulent flame structure of oxyfuel syngas at high pressure up to 1.0 mpa. *Hy. Energy*, 44:11185–11193.

[51] Wang, J., Matsuno, F., Okuyama, M., Ogami, Y., Kobayashi, H., and Huang, Z. (2013). Flame front characteristics of turbulent premixed flames diluted with co2 and h2o at high pressure and high temperature. *Proc. Combust. Inst.*, 34:1429–1436.

[52] Wang, J., Yu, S., Zhang, M., Jin, W., Huang, Z., Chen, S., and Kobayashi, H. (2015). Burning velocity and statistical flame front structure of turbulent premixed flames at high pressure up to 1.0 mpa. *Exp Thermal and Fluid Sci.*, 68:196–204.

[53] Wang, X., Jin, T., Xie, Y., and Luo, K. (2018a). Effects of pressure and karlovitz number on the turbulence-flame interactions in lean premixed h2/air flames. *Fuel*, 235:1293–1300.

[54] Wang, X., Jin, T., Xie, Y., and Luo, K. (2018b). Pressure effects on flame structures and chemical pathways for lean premixed turbulent h2/air flames: Three-dimensional dns studies. *Fuel*, 215:320–329.

[55] Wang, Z. and Abraham, J. (2018). Effects of karlovitz number on flame surface wrinkling in turbulent lean premixed methane-air flames. *Combust. Sci. Technol.*, 190(3):363–392.

[56] Yang, S., Ranjan, R., Yang, V., Menon, S., and Sun, W. (2017a). Parallel on-the-fly adaptive kinetics in direct numerical simulation of turbulent premixed flame. *Proceedings of the Combustion Institute*, 36(2):2025–2032.

[57] Yang, S., Ranjan, R., Yang, V., Sun, W., and Menon, S. (2017b). Sensitivity of predictions to chemical kinetics models in a temporally evolving turbulent non-premixed flame. *Combustion and Flame*, 183:224–241.

[58] Yilmaz, B. and Gokalp, I. (2017). Analysis of turbulent lean premixed methane-air flame statistics at elevated pressures. *Energy Fuels*, 31:12815–12822.

[59] Yuen, F. and Gülder, Ö. L. (2009). Investigation of dynamics of lean turbulent premixed flames by rayleigh imaging. *AIAA J.*, 47:2964–2973.

[60] Zhou, B., Brackmann, C., Wang, Z., Li, Z., Richter, M., Aldén, M., and Bai, X.-S. (2017). Thin reaction zone and distributed reaction zone regimes in turbulent premixed methane/air flames: Scalar distributions and correlations. *Combust. Flame*, 175.

VITA

Jamie Bowers was born in 1994 in Alabama to Dr. James and Mrs. Laura Bowers. She attended the University of Tennessee at Chattanooga, where she studied applied mathematics and mechanical engineering. During her undergraduate education, she was elected membership to the U.S. honorary national mathematics society, Pi Mu Epsilon, received a first-place design award from the American Society of Engineering Education, and dedicated countless hours to tutoring her peers in mathematics and engineering. In May 2019, Jamie graduated with a Bachelor of Science in Applied Mathematics. In August of that same year, she was accepted to The Graduate School at the University of Tennesse at Chattanooga to continue her education in mechanical engineering. During her graduate studies, she has researched modeling and simulation of turbulent combustion under the supervision of Dr. Reetesh Ranjan. In August 2021, Jamie graduated from the University of Tennessee at Chattanooga with a Master of Science in Mechanical Engineering-Energy.